KU LEUVEN

TECHNISCHE UNIVERSITÄT DRESDEN

Construction of a measurement instrument for magneto-optical and magneto-thermoelectric characterization of magnetic spin textures in micro- and nanostructures

Mauricio José Bejarano Rodríguez

Thesis submitted for the degree of
Erasmus Mundus Master of Science
in Nanoscience and Nanotechnology

Thesis supervisor:
Dr. rer. nat. Helmut Schultheiss

Assessors:
Prof. dr. rer. nat. Jürgen Fassbender
Prof. dr. Joris Van de Vondel

Academic year 2017 – 2018

© Copyright KU Leuven

Without written permission of the thesis supervisor and the author it is forbidden to reproduce or adapt in any form or by any means any part of this publication. Requests for obtaining the right to reproduce or utilize parts of this publication should be addressed to Faculteit Ingenieurswetenschappen, Kasteelpark Arenberg 1 bus 2200, B-3001 Heverlee, +32-16-321350.

A written permission of the thesis supervisor is also required to use the methods, products, schematics and programmes described in this work for industrial or commercial use, and for submitting this publication in scientific contests.

Contents

Abstract

The magneto-optical Kerr effect is a surface sensitive technique to characterize magnetic materials. It consists of an induced rotation and ellipticity of the polarization plane of the light after reflection from a magnetic surface. The overall effect is proportional to the magnetization of the sample. A measurement instrument based on this technique is presented. It provides a fast, reliable, and sensitive way of characterizing the magnetic spin textures in state-of-the-art magnetic micro- and nanostructures. Moreover, the instrument allows for simultaneous measurement of the magneto-thermal properties of magnetic nanostructures, thus enhancing the range of possible applications. The setup was tested for magneto-optical and magneto-thermoelectric characterizations on the Weyl semimetal Co_2MnGa and for spatial resolution on Pt/CoFeB nanowires.

List of Figures and Tables

List of Figures

List of Tables

Chapter 1

Introduction

The technologies that helped sustain Moore's Law in the 20th century fostered the advancement of many new research fields in science. The newly discovered capabilities of controlling with nanometer precision the growth of different layers of materials enabled scientists around the globe to start investigating the physics that govern this nanoworld. One of the fields that benefitted from this was magnetism. Before the nanofabrication technologies existed, the study of magnetism was secluded to bulk materials. Quantum theory and the discovery of the spin had set the foundations for a quantum theory of magnetism, however, experimental studies were limited by the available technology. However, with the rapid progress of thin film deposition and optical lithography soon scientists were able to start unveiling the nanoscopic physics of magnetism, thus giving birth to the field named nanomagnetism. This field is behind the invention of the magnetic storage and sensing technologies that exist nowadays. A good example is the magnetoresistive random access memory (MRAM) introduced into the markets in the 1990s. However, the ongoing advances with the miniaturization trend are bringing upon new challenges not faced before. The phenomena being studied are constantly getting smaller and smaller which makes it intrinsically more difficult to detect and measure. Thus, this demands for experimental techniques that can meet the harsh requirements of the nanoworld and help reveal its secrets. The aim of this work is to present an experimental tool to meet the ever increasing demands and complexity of nanomagnetism research. The tool presented allows studying magnetic spin textures in the micro- and nanoscale, which will help provide insights into domain wall dynamics and magneto-thermal phenomena. As such it could help contribute to research projects in the subfields of magnonics, spintronics, and spin-caloritronics. Built upon the principle of the magneto-optical Kerr effect, it is a fast, non-contact, precise, and reliable technique to simultaneously characterize the magneto-optical and magneto-thermoelectric properties of magnetic (hybrid)-nanostructures. The ultimate goal is to help researchers understand the physics that govern magnetic micro- and nanoscale textures and dynamics.

The organization of this thesis is as follows:

Chapter 2 presents the magneto-optical Kerr effect theory that underlies the functionality of the experimental setup. The anisotropic magnetoresistance effect

(AMR), ordinary and anomalous Nernst effect (ONE and ANE), and the anisotropic magneto-thermpower (AMT) are also discussed as they provide a better framework to understand the study case applications that were used to test the setup.

Chapter 3 provides a detailed view on the design, construction, characterization, and operation of the experimental setup.

Chapter 4 examines two study case applications used to benchmark the experimental tool. The underlying physics of these applications are also analyzed and discussed.

Finally, the conclusions and future work are presented in chapter 5.

*A brief remark on the aim of this work: initially it was planned to use this thesis work to study magnetic spin textures in spin-Hall nano-oscillators. The experimental tool here presented was thus initially planned to study this topic via magneto-transport and magneto-optical characterizations in metal/ferromagnet nanowires. However, this was not possible due to unforeseen complications during the period that comprised the thesis work and, therefore, the focus was redirected towards the construction of the experimental tool and studying magnetic spin textures in another type of material. This was possible due to a collaboration project with a research group from the Institut für Festkörper- und Materialphysik from the Technische Universität Dresden. This collaboration provided the ideal scenario for testing the setup and studying magneto-thermal phenomena on Weyl semimetals. As a result, the focus of the master thesis had to be slightly changed towards a related but different topic.

Chapter 2

Theory

The main purpose of this chapter is to present the theoretical foundation on which the MOKE microscopy technique is based on. Therefore, most of the attention will be centered on explaining the working principle of this effect and its application as a modern experimental technique. Combining laser scanning microscopy with magneto-electric (-thermal) transport measurements allows for characterizing magnetic micro- and nanostructures with lateral resolution down to the nanometer range, in a non-invasive and precise way. Thus, being able to use MOKE simultaneously with magneto-transport measurements could be a very powerful tool for studying the modern and challenging physics being tackled in the field of nanoscience.

The organization of the chapter is as follows: on section 2.1 the magneto-optical Kerr effect is presented and discussed. The anisotropic magnetoresistance effect and spin-caloritronic effects are explained in sections 2.2 and 2.3, respectively, as they are relevant for understanding the application projects included in chapter 4.

2.1 Magneto-optical Kerr effect

2.1.1 Introduction

The study of the interaction between light and magnetism was of great interest in the first half of the 19th century. The works of the experimentalist Michael Faraday and the theorist James Clerk Maxwell set the foundations of classical electromagnetism theory. In 1845 Faraday discovered that light suffers a polarization change when it is transmitted through a transparent, magnetized material. In 1876 the Scottish physicist John Kerr discovered the same effect but in the reflection of light. This effect is called the magneto-optical Kerr effect (MOKE) in his honor and is now one of the most powerful tools in laboratories around the world investigating the properties of magnetic materials. Moreover, it forms the basis of the magneto-optical recording technology that underlies the magneto-optical drives that hit the market in the late 1980s and early 1990s [19]. MOKE is a very useful research tool for the study of magnetic thin films as it can provide spatial resolutions near the diffraction limit of light (200 nm)[19]. It is a surface-sensitive technique that allows probing the magnetization within the skin-depth region, which could be 10-20 nm in most

metals [4]. Furthermore, it is relatively easy and straightforward to implement, in contrast to the more expensive and complex alternatives [29]. However, its biggest advantage is its capacity to probe ultrafast magnetization dynamics with the use of short and intense pulse lasers [17].

The magneto-optical Kerr effect is the central part of the setup built on this thesis and due to its importance a detailed discussion of its fundamental principles follows in the next sections. However, before addressing MOKE in itself, a brief overview of light is presented, as it is one of the key participants in this magneto-optical effect.

2.1.2 Polarization of light

From Maxwell's theory derives the idea that light is an electromagnetic wave [19]. It is made up of transverse electric and magnetic fields traveling along a propagation direction. Equations 2.1 and 2.2 come from Maxwell's equations and describe the travelling electric and magnetic field respectively. Figure 2.1 shows an illustration of an electromagnetic wave [19].

$$\mathbf{E}(\mathbf{r},t) = \epsilon_p E_0 e^{i(\mathbf{k}\cdot\mathbf{r}-\omega t)} \tag{2.1}$$

$$\mathbf{B}(\mathbf{r},t) = \frac{1}{c}(\mathbf{k}_0 \times \epsilon_p) E_0 e^{i(\mathbf{k}\cdot\mathbf{r}-\omega t)} \tag{2.2}$$

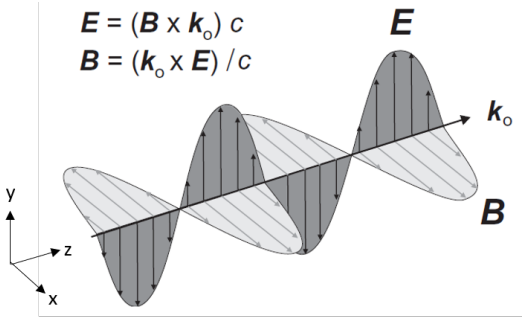

Figure 2.1: Schematic view of a traveling electromagnetic wave. The electric and magnetic field are transverse to each other and to the propagation direction $\mathbf{k}_0$. The electric field vector is named the polarization vector as it defines the polarization state of the electromagnetic wave. Taken from [19].

In equations 2.1 and 2.2 the term ϵ_p is the unit polarization vector and $\mathbf{k} = (\omega/c)\mathbf{k}_0$ is the wave vector along the propagation direction. The electric field vector is called the polarization vector as it defines the state of the polarization of the electromagnetic wave. Natural light is called *unpolarized* because the electric field vector consists of a rapid sucession of different polarization states lying in the x-y plane [19]. This means that at any given time, the electric field vector can have different orientations on this plane. When the electric field vector has a defined orientation on the plane perpendicular to the propagation direction the electromagnetic wave is considered

to be *linearly polarized*. Other possible configurations are circular and elliptical polarizations. The possible polarizations of light are shown in figure 2.2.

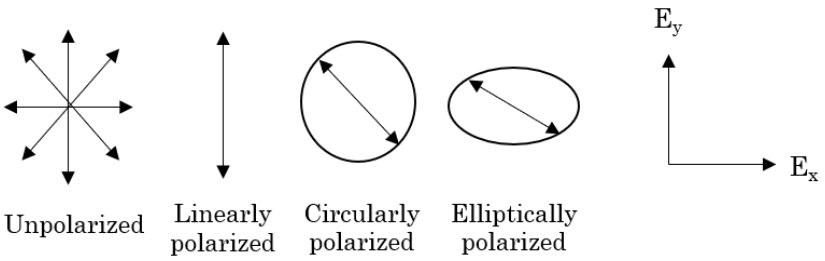

Figure 2.2: Possible polarization states of light.

When light impinges on a surface, the vectors along the propagation direction of the incoming and reflected beams define the plane of incidence of the light, sometimes called the scattering plane [12]. If the light is linearly polarized on the plane of incidence, the light is called p-polarized (from parallel). If light is linearly polarized perpendicular to the plane of incidence, it is called s-polarized (from the german *senkrecht*). Figure 2.3 illustrates these polarization directions relative to the plane of incidence.

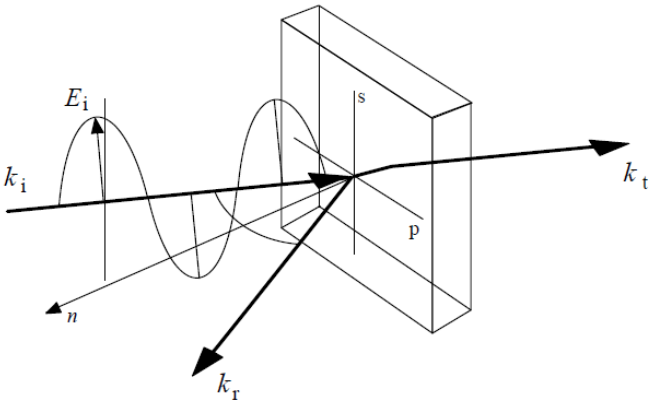

Figure 2.3: Light being refracted from a medium, with the s- and p-polarization directions defined. The vector $\mathbf{k}_i$ and $\mathbf{k}_r$ define the plane of incidence. Taken from [12].

2.1.3 Definition of the magneto-optical Kerr effect

When s- or p-polarized light impinges on a magnetic surface it experiences a rotation of its polarization plane and becomes elliptically polarized [19]. These two consequences, named Kerr rotation and Kerr ellipticity, make up the magneto-optical Kerr effect. Figure 2.4 shows these effects.

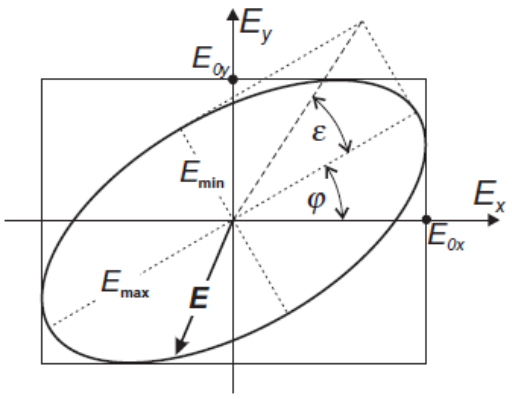

Figure 2.4: Electric field vector after a linearly polarized light impinges on a magnetic surface and experiences the Kerr effect. The angle φ is called the Kerr rotation and the angle ε is called the Kerr ellipticity. Taken from [19].

The angle φ in figure 2.4 represents the Kerr rotation and denotes the rotation of the major axis with respect to its original polarization direction. In figure 2.4 the initial polarization direction was along the x axis. The Kerr rotation is given by equation 2.3.

$$\tan 2\varphi = \frac{2E_{0x}E_{0y}\cos\phi}{E_{0x}^2 - E_{0y}^2} \tag{2.3}$$

The terms E_{0x} and E_{0y} denote the electric field amplitudes of the linearly polarized light in the x and y directions [19]. ϕ is the phase difference between these amplitudes.

The angle ε in figure 2.4 is the ratio between the normal components of the resulting elliptical polarized light [19]. It is called the Kerr ellipticity and is given by

$$\tan\varepsilon = \frac{|\mathbf{E}_{min}|}{|\mathbf{E}_{max}|} = \frac{|E_{0R} - E_{0L}|}{|E_{0R} + E_{0L}|} \tag{2.4}$$

The terms E_{0R} and E_{0L} are the basis states of the right-circularly polarized light and left-circularly polarized light respectively. MOKE is often represented by the complex Kerr angle, Θ_K, given by equation 2.5 [24].

$$\Theta_K = \varphi + i\varepsilon \tag{2.5}$$

2.1.4 Physical origin

To explain why the Kerr effect takes place it is best to picture linearly polarized light as a linear combination of the circularly polarized basis states, that is, E_{0R} and E_{0L} for right-handed and left-handed circular polarizations respectively. The interaction of these components with matter results in the Kerr rotation and Kerr ellipticity, however, these effects have different physical origins.

The physical origin of the Kerr rotation can be explained in a macroscopical approach. When light travels through a dielectric material it may experience different refractive indexes depending on the direction of propagation. In general, if a material is optically isotropic, then the permittivity tensor looks like equation 2.6.

$$\epsilon(\omega) = \begin{pmatrix} \epsilon_{xx} & 0 & 0 \\ 0 & \epsilon_{yy} & 0 \\ 0 & 0 & \epsilon_{zz} \end{pmatrix} \tag{2.6}$$

However, if the material is optically anisotropic (as in when there is a net volume magnetization), the permittivity tensor has non-zero off-diagonal terms and looks like equation 2.7 [40].

$$\epsilon(\omega) = \begin{pmatrix} \epsilon_{xx} & \epsilon_{xy} & -\epsilon_{xz} \\ -\epsilon_{xy} & \epsilon_{yy} & \epsilon_{yz} \\ \epsilon_{xz} & -\epsilon_{yz} & \epsilon_{zz} \end{pmatrix} \tag{2.7}$$

The off-diagonal terms are dependent on the magnetization, and affect the velocity and attenuation of light in these particular directions. As a consequence left-circularly polarized (LCP) light and right-circularly polarized (RCP) light experience different refractive indices thus traveling with different velocities within the material. When they come out of the material they will have a phase difference and after recombination this will be evidenced in a rotation of the polarization plane.

The origin of the Kerr ellipticity relies on the magnetic circular dichroism effect [19]. This effect accounts for the asymmetric absorbtion of left and right circularly polarized light. When circularly polarized light impinges on a magnetic sample, due to the conservation of angular momentum and the selection rules for electron dipole transitions, it transfers the photon angular momentum to the electrons on the core shells via spin-orbit coupling (in spin-orbit split levels) thus spin-polarizing them. As a second step, the photons excite them to the higher-energy unfilled valence shells. However, as in ferromagnets the unfilled d-band is spin-split between up- and down-spin with different hole density of states, then the capture of the excited photoelectrons will be asymmetric. That is, the capturing of the photoelectron on the d-shell will depend on the spin angular momentum of the excited photoelectron. The overall result is that in ferromagnetic materials there will be a preferential absorption of one of the circularly-polarized directions. Figure 2.5 shows the magnetic circular dichroism effect.

2.1.5 MOKE geometries

There are three main geometries in MOKE experiments: longitudinal MOKE (LMOKE), polar MOKE (PMOKE) and transverse MOKE (TMOKE), according to the direction of the magnetization. These geometries are shown in figure 2.6.

In the polar and longitudinal geometries, s- or p- polarized light will transform into elliptically polarized light, due to the Kerr rotation and ellipticity effects. However, in transverse MOKE light experiences no Kerr rotation or ellipticity at all, only a

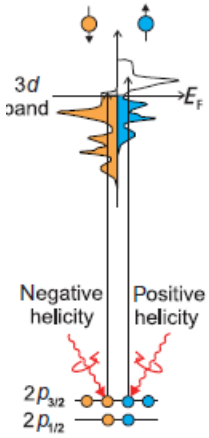

Figure 2.5: Magnetic circular dichroism effect. Photons with opposite angular momentum excite electrons from spin-orbit split bands to the upper d bands. The different density of states of holes in the d bands results in an asymmetric absorption of left- and right-circularly polarized light. Taken from [19].

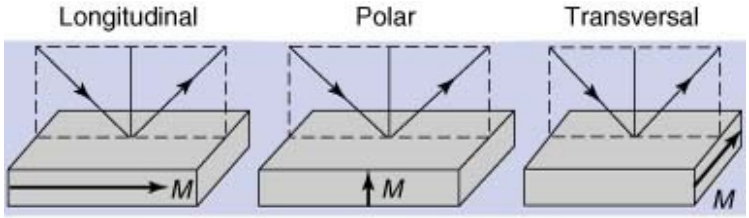

Figure 2.6: MOKE measurement geometries showing the incoming and reflected light beam, the incidence plane and the magnetization direction. Taken from [21].

change in intensity. Polar MOKE is generally an order of magnitude larger than longitudinal MOKE [2].

2.2 Anisotropic magnetoresistance

2.2.1 Background

In 1856 William Thomson, later known as Lord Kelvin, discovered that the resistance of an iron conductor changed when submitted to an external magnetic field [19]. Specifically, he noticed that when the magnetic field is applied along the conductor the resistance increased by 0.2% and when the field was perpendicular the resistance decreased by 0.4%. What Lord Kelvin had discovered was the effect called magnetoresistance, namely, the change of resistance of a material under the influence of an external magnetic field. For the sake of correctness, Lord Kelvin's experiment was the first scientific record of the anisotropic magnetoresistance effect (AMR), one of the many magnetoresistance effects that have been discovered since

then, and the one which is the main topic of this section.

2.2.2 Description

The AMR effect is defined as the change in resistance of a material when the magnetic field is rotated in an angle θ along the plane of the current travelling through this material. This is shown in figure 2.7.

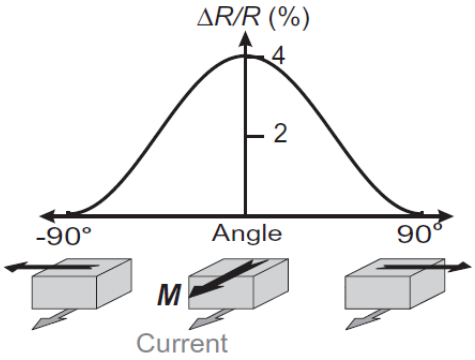

Figure 2.7: Illustration of the AMR effect in a ferromagnetic material. Displayed is the resistance change as a function of the angle between the magnetization and the current direction. The high resistance state is experienced when the magnetization and the current are parallel to each other, and the low resistance state when they are perpendicular. Taken from [19].

Defining the resistance of the material when the magnetization and the current are parallel to each other as $R_{\parallel}$, and when they are perpendicular as $R_{\perp}$, then the AMR effect is defined as in equation 2.8 [19].

$$\frac{\nabla R}{R_{\text{avg}}} = \frac{R_{\parallel} - R_{\perp}}{(R_{\parallel} + 2R_{\perp})/3} \tag{2.8}$$

The usual way to describe AMR, however, is as a function of the angle θ between the magnetization and the current direction. This description is represented by equation 2.9 [32].

$$R(\theta) = R_{\perp} + (R_{\parallel} - R_{\perp}) \cos^2 \theta \tag{2.9}$$

2.2.3 Physical origin

The microscopic origin of the AMR effect is thought to be solely the spin-orbit coupling [33]. However, before explaining how this effect influences the resistivity of a ferromagnetic material, the Mott description of electrical transport in ferromagnets has to be addressed first.

Mott suggested in 1936 that in ferromagnetic metals the electrical conduction is provided by the dispersed s electron band and the magnetic properties are defined

by the localized d band [25]. In this picture the scattering process comes from s electrons jumping to the d band. However, the scattering is spin selective, meaning that electrons can only jump to empty d states with the same spin. Spin-flipping events were considered negligible. This proposal together with Fermi's Golden Rule cemented the foundations for the "two current model" in ferromagnets, in which the current is carried by separate spin-channels, without much interaction between them [14]. Fermi's Golden Rule states that the scattering probability is proportional to the amount of empty final states that the electron can scatter to [13]. Given the fact that in ferromagnets the d bands are exchange-split and filled differently at the Fermi level, this meant that the scattering rates for electrons of opposite spin polarization are different, which eventually leads to the preferential loss of one spin component. The two current model is illustrated in figure 2.8.

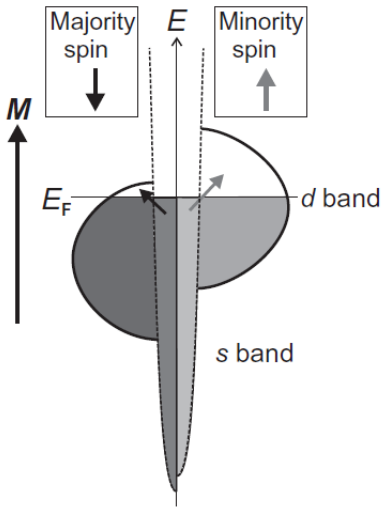

Figure 2.8: Illustration of the two current model. There are more empty d states for the electrons in the minority band, hence, experiencing a greater scattering probability than spin-down electrons in the majority band. This means that the channel for the spin-up electrons (minority) has greater resistivity. Taken from [19].

Having this transport model in mind, it is now easier to explain the microscopic origins of the AMR effect. From the two current model it can be said that the empty minority d states, $N_h^{\uparrow}$, determine directly the magnetic moment $|\mathbf{m}|$ [19]. Thus, the resistance of a ferromagnet can be written as equation 2.10.

$$R = R_0 + R_{\uparrow} = R_0 + N_h^{\uparrow} = R_0 + |\mathbf{m}| \tag{2.10}$$

The term R_0 is isotropic, however, in materials with spin-orbit coupling the term $|\mathbf{m}|$ is not. When applying a magnetic field at an angle with respect to the current direction, there is a spin-subband intermixing which changes the amount of $N_h^{\uparrow}$, and hence $|\mathbf{m}|$, for every angular position [19]. This change in the availability of the final d states originates the AMR effect.

Another helpful way of picturing the AMR effect is given by figure 2.9. On 2.9a the microscopic view when the magnetic field is perpendicular to the current is shown. In this configuration, following the explanation given before, it can be interpreted that there are less available d states to scatter to, as the cross section is small for the incoming conduction electrons [32, 31]. Therefore, the resistance state is low. In 2.9b, the magnetic field has been aligned parallel to the current and because of spin-orbit coupling, the electron orbital distribution also changes. The resulting orbital configuration has a larger cross section for the incoming electrons, thus increasing the availability of final d states the conduction electrons can scatter to. As a result, this configuration yields a higher resistance state.

(a)

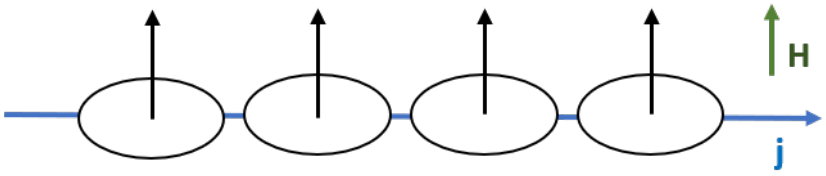

(b)

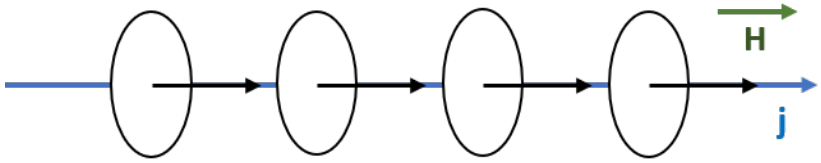

Figure 2.9: Microscopic view of the AMR effect. The atoms are represented by the orbital distribution (the ovals) and the atomic magnetic moment (the black arrow). Notice that for 3d metals there is no spherical symmetry in the orbitals. (a) Orbital distribution when magnetic field is aligned perpendicularly to the current. The scattering cross section is reduced, so there are less available d states to scatter to. As a result the resistance state is low. (b) Orbital distribution when magnetic field is aligned parallel to the current. The scattering cross section is increased, so there are more available d states to scatter to. As a result the resistance state is high.

2.3 Spin caloritronics

Spin caloritronics is a young research field that relates spin or magnetization transport to heat transport in micro- and nanostructures. It has gathered much attention from the scientific community in the past 10 years due to the promising possibilities of delivering thermal-to-electrical energy conversion solutions for waste heat recovery and temperature control problems [5]. Additionally, considering that power consumption is constantly threatening to limit Moore's Law, spin caloritronics might be a way to use the dissipating power into more processing capacity, thus helping tackling two problems at once.

In this section an overview of selected known thermal transport effects is presented. Some effects will be further discussed into more detail as they are more relevant to the study case applications included in chapter 4.

2.3.1 Overview of thermal transport effects

In a generalized view, thermal transport occurs when heat is transferred as a result of non-equilibrium thermodynamic effects [5]. The transport of heat can occur via (quasi-) particles: electrons, magnons or phonons which in turn depend on the type of material where the effect is taking place. For example, electrons can drive thermal transport in metals and magnons in ferromagnetic insulators. Due to the great variety of factors involved, there are many types of thermal transport effects. Furthermore, these effects can be measured in a wide range of geometric configurations. The most used configurations are shown in figure 2.10.

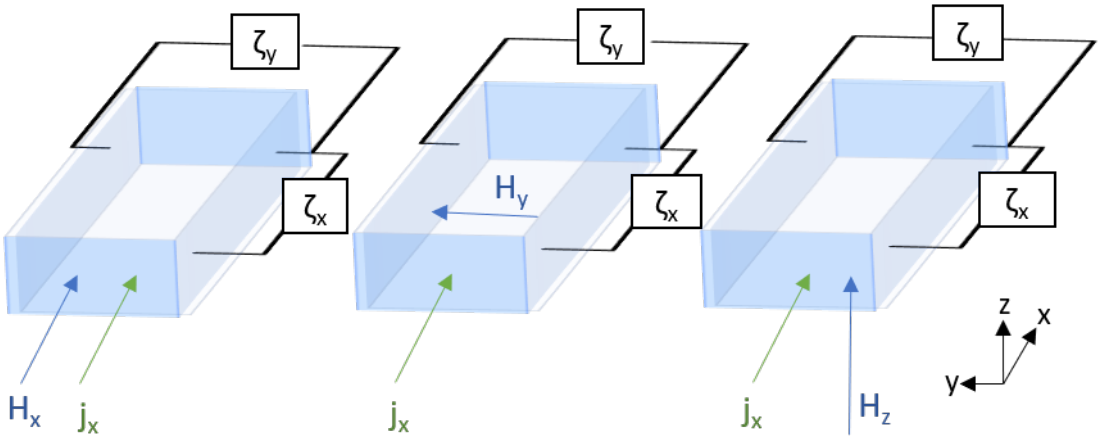

Figure 2.10: Measurement geometries for thermal transport effects. The flux, whether a thermal current j_Q or a charge current j_C, is shown in the x direction. ζ stands for a generic thermodynamic force, $\mathbf{E}$ or ∇T. The permutations on the magnetic field direction and the type of current applied results in a wide variety of transport effects.

Table 2.1 shows some spin-dependent and spin-independent caloritronic effects. Given the wide range of thermal-transport phenomena, attention will be centered on just a few of them, which are discussed to more detail in the following sections.

2.3.2 Ordinary Nernst Effect

The ordinary Nernst effect (ONE) is a spin-independent transport phenomena that takes place in metallic materials. It is caused by a thermal flux which travels perpendicularly to an applied magnetic field and creates a transverse voltage. It is the analogous effect to the ordinary Hall effect. The schematic of ONE is shown in figure 2.11.

Table 2.1: List of selected magneto-thermal effects.

Effect	Material	Field	Input	Output
Longitudinal AMT [a]	Metals	H_x	$\nabla_x T$	E_x
Transverse AMT [a]	Metals	H_y, H_z	$\nabla_x T$	E_x
Planar Nernst	Metals	H_y	$\nabla_x T$	E_y
Ordinary Nernst	Metals	H_z	$\nabla_x T$	E_y
Anomalous Nernst	Ferromagnetic metals	H_z	$\nabla_x T$	E_y
Ettingshausen	Metals	H_z	$j_{c,x}$	$\nabla_x T$
Spin-dependent Seebeck	Ferromagnetic metals	-	$\nabla_x T$	E_x
Spin Seebeck	Ferromagnet/Metal	-	$\nabla_x T$	$E_{\mathrm{ISHE,y}}$ [b]

[a] Anisotropic magneto-thermopower
[b] The electrical output is detected by means of the inverse spin-Hall effect in the metallic layer.

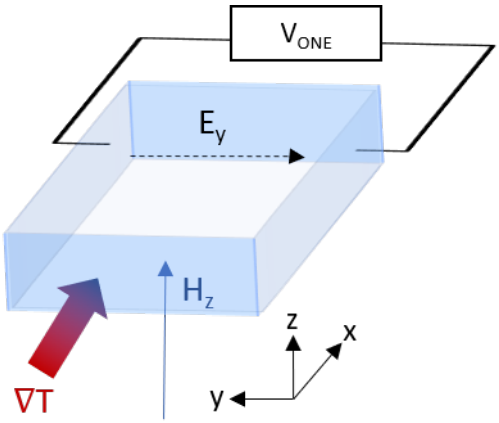

Figure 2.11: Schematic illustration of the ordinary Nernst effect.

The microscopic origin of the ordinary Nernst effect is due to the Lorentz force acting on the conducting electrons carrying the thermal flux. This force has a form of $\mathbf{F}_L = \mathbf{v}_q \times \mathbf{B}$ and thus acts perpendicularly to the propagation direction of the heat carriers, deflecting them from their path and creating a charge accumulation that builds up an electric field. This electric field exactly balances the Lorentz force and is the measured quantity in this type of measurement.

2.3.3 Anomalous Nernst Effect

As seen in Table 2.1 the anomalous Nernst effect (ANE) occurs in a ferromagnetic metal when a thermal flux travels perpendicular to an applied magnetic field creating a transverse electric field, named the anomalous Nernst voltage [36]. It is a spin-dependent process as it is based on the spin-polarized charge current occuring in ferromagnetic metals, and explained with the Stoner model of ferromagnetism. This model is at the core of the two current model presented in section 2.2 and illustrated in figure 2.8. It assumes that charge carriers in ferromagnetic metals split in spin-up and spin-down d bands with different density of states at the Fermi level such that

$\mu_\downarrow \neq \mu_\uparrow$. It is precisely this inequality that creats an imbalance in the concentration of charge carriers of different spin polarizations, thus creating a spin-polarized current, that is $j_{C\uparrow} \neq j_{C\downarrow}$. This means that the charge current will carry at the same time a net spin flux [5].

The general measurement schematic is shown in figure 2.12. The local anomalous Nernst effect is given by equation 2.11. In this equation, $\mathbf{E}_{\mathrm{ANE}}$ is the transverse electric field perpendicular to the magnetization $\mathbf{M}$ of the material and the thermal gradient ∇T. N is named the Nernst coefficient. As explained before, in the transverse direction there will be a charge accumulation concomitant with a spin accumulation.

$$\mathbf{E}_{\mathrm{ANE}}(x,y) = -N\mu_0 \mathbf{M}(x,y) \times \nabla T(x,y) \tag{2.11}$$

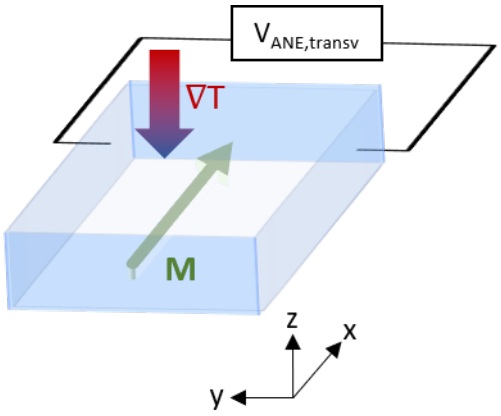

Figure 2.12: Schematic illustration of the anomalous Nernst effect.

The physical origins of the ANE have not been analyzed to great detail yet, but scientists think it could be originated by the same processes that create the analogous anomalous Hall effect [5]. These processes are either from extrinsic sources, as impurity scattering events, or intrinsic sources, as band structure effects. These processes are:

i Skew scattering: the charge carriers experience spin-dependent asymmetric scattering with the localized impurity states [7].

ii Side-jump mechanism: the path of the conducting electrons is deviated due to local distortions of the electron wave functions as a result of spin-orbit interactions [3].

iii Berry phase: intrinsic topological phases in the band structure induce a phase difference, which can be thought of an emergent magnetic field acting on the charge carriers [20].

In a ferromagnetic metal, when a thermal gradient is applied under a perpendicular magnetic field, the part of the transverse Nernst voltage that arises that is proportional

to H_z comes from the ordinary Nernst effect and the part that is proportional to $\mathbf{M}$ comes from the anomalous Nernst effect. This allows using the anomalous Nernst effect to measure the component of magnetization along a certain direction only taking into account that $E_{\mathrm{ANE}}(-\mathbf{M}) = -E_{\mathrm{ANE}}(\mathbf{M})$.

2.3.4 Anisotropic magneto-thermopower

The anisotropic magneto-thermopower is the thermal counterpart of the anisotropic magnetoresistance effect. It is obtained by subtituting the input current j_x by a thermal gradient ∇T_x and applying a magnetic field in the same plane of the thermal gradient. The electric field that arises depends on the angle φ_T between the magnetic field and the direction of the thermal gradient. Figure 2.13 shows the geometry of an experiment measuring this effect.

Equation 2.12 describes the anisotropic magneto-thermopower with φ being the angle between the magnetic field and the x axis, and φ_T the angle between ∇T_x and the magnetic field. $S_\perp$ and $S_\parallel$ are the Seebeck coefficients when the magnetic field is perpendicular and parallel to the thermal gradient respectively [31].

$$\mathbf{E}_{\mathrm{AMT}} = -\left(\frac{S_\parallel + S_\perp}{2} - \frac{S_\parallel - S_\perp}{2}\sin 2\varphi\right)|\nabla T|\cos\varphi_T \tag{2.12}$$

The physical origins of AMT are believed to be of the same nature as of AMR [5].

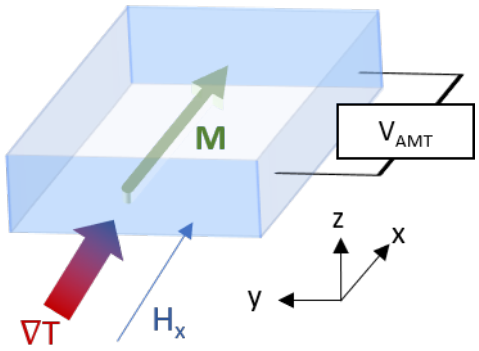

Figure 2.13: Schematic illustration of the anisotropic magneto-thermopower.

Chapter 3

Experimental setup

This chapter comprises the central part of this work: the design, construction, and characterization of the experimental setup. The main goals of the tool were to perform (L+P)-MOKE measurements and magneto-thermal characterizations of magnetic micro- and nanostructures, while ensuring nanometer-precision spatial resolution, low signal-to-noise ratio, and high reliability. The setup also needed to be able to support 4-point resistance measurements for high-precision detection of magnetoresistance effects and AC connections for dynamic measurements.

The chapter is organized as follows: section 3.1 presents the design and general requirements for the setup. In section 3.2 the optical system and all its components are discussed in detail. The lock-in detection mechanism used for the signal acquisition is explained in section 3.3. In section 3.4 the spatial resolution of the tool is discussed and, finally, in section 3.5 the software suite used to operate the setup is presented.

3.1 Overview

The major hardware requirements of the setup are shown in the diagram in figure 3.1. These requirements are: signal acquisition for both the electrical (Nernst/magnetoresistance effects) and the optical (MOKE) signals, a viewing system for contacting and measuring the sample, DC and AC current source availability, a nano-precision positioning system, laser and magnetic field availabilities, and the capacity to constantly control and measure the magnetic field.

The hardware components are shown in the schematic of figure 3.2. Figures 3.3 and 3.4 show sideviews of the finalized 3D models of the nanopositioning stage system and the magnet in measuring position. In the following sections each major hardware component is introduced.

3.1.1 Hardware components

Current source

The current source used is the Keithley model 6221. This unit has capabilities of delivering AC and DC currents ranging from 100 fA to 100 mA. The current is

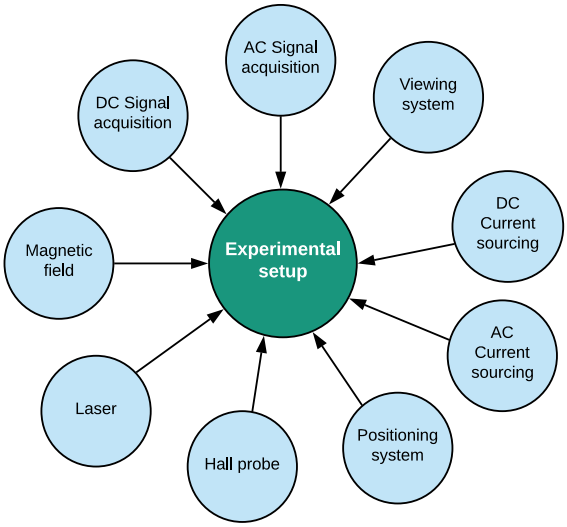

Figure 3.1: Main hardware requirements for the experimental setup.

injected to the sample via 5 μm diameter tungsten tips from Signatone.

Field monitoring

The magnetic field is constantly measured by the 475 DSP Gaussmeter from Lake Shore Cryotronics. It has full-scale ranges from 35 mG to 350 kG. The Hall probe is

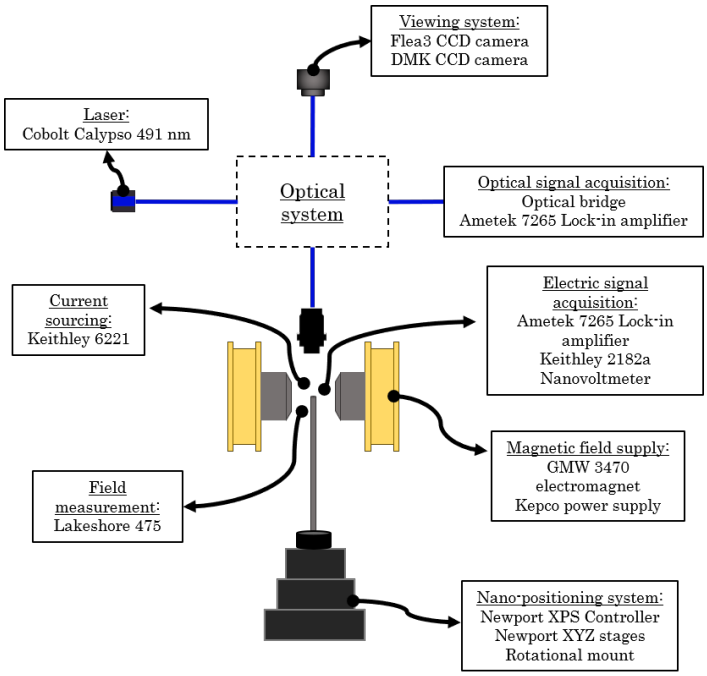

Figure 3.2: Hardware schematic of the setup.

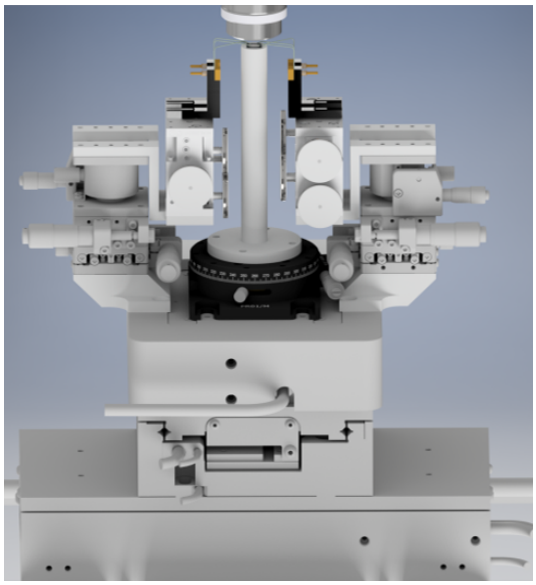

Figure 3.3: Computer model of the nanopositioning system including the rotary stage for the sample holder and the micrometer-precision xyz stages for controlling the probes. The setup has support for up to 4 DC probes, and 2 microwave picoprobes (not shown in the image). Moreover, 6 xyz stages provide the necessary degrees of freedom for manipulating the DC and AC probes.

located next to one of the magnet poles. A calibration procedure calculates the link factor between the measured fields at the sample and at the magnet pole position.

Laser

The laser source used is a Cobolt Calypso^{TM}491 nm wavelength continuous-wave diode pumped laser. This laser has a maximum nominal output power of 200 mW, however, normal operating powers were below 20 mW. The laser beam is linearly polarized on the vertical direction and has a diameter of 700 μm at the aperture.

Viewing system

The viewing system is split into two subsystems: one for contacting the sample with the probes and one for viewing during measurement runtime. The viewing system for measuring is included in the optical system which will be discussed in the next section. The contacting viewing system is shown in figure 3.5 and consists of a CCD camera from ImagingSource model DMK 31AF03 and a blue LED source coupled by a 50:50 beamsplitter cube. The lens used is a Computar Telecentric 55 mm lens with a working distance of 140 mm.

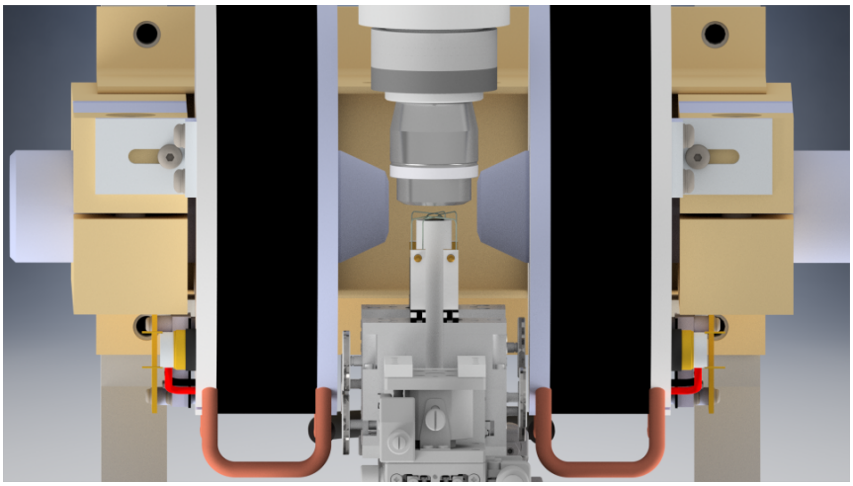

Figure 3.4: Computer model for the magnet in measuring position. The magnet slides into this position so that the sample holder is exactly in the middle of the poles and below the microscope objective.

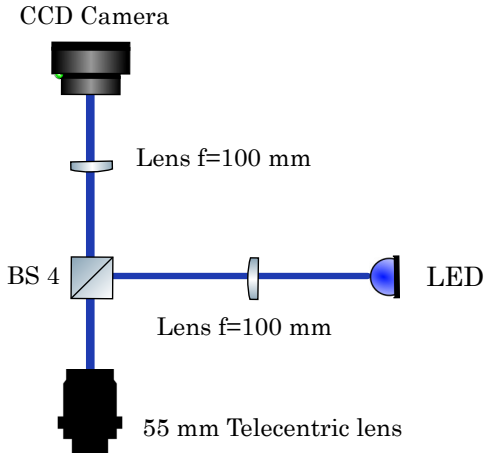

Figure 3.5: Contacting viewing system. BS stands for beam-splitter cube. A blue LED from Thorlabs was used. The contacting system is completely separated from the measuring optical system.

Magnetic field supply

The magnetic field is provided by a water-cooled GMW 3470 dipolar electromagnet. The magnet poles have a 20 mm diameter and are separated by a gap of 40 mm. With this gap the magnet can provide up to 380 mT. The power supply of the electromagnet is a Kepco BOP 100-10MG.

Positioning system

The positioning system relies on the XM Ultra-Precision linear motor stages series from Newport. These stages provide the nanometer-reliable motion for measuring nano-sized magnetic structures. The x stage is model XMS160-S with a travel range of 160 mm. The y stage is model XMS50-S with a travel range of 50 mm. Both of these linear stages have a minimum incremental motion of 10 nm. The vertical z stage is model VP-5ZA with a 4.8 mm travel range and a minimum incremental motion of 60 nm. These stages are controlled by the Newport XPS-Q8 controller. Additionally the sample holder is mounted on a Thorlabs PR01/M rotational stage that allows for diverse measurement angles.

3.1.2 Equipment connection

Figure 3.6 shows the connection of the hardware to the laboratory workstation.

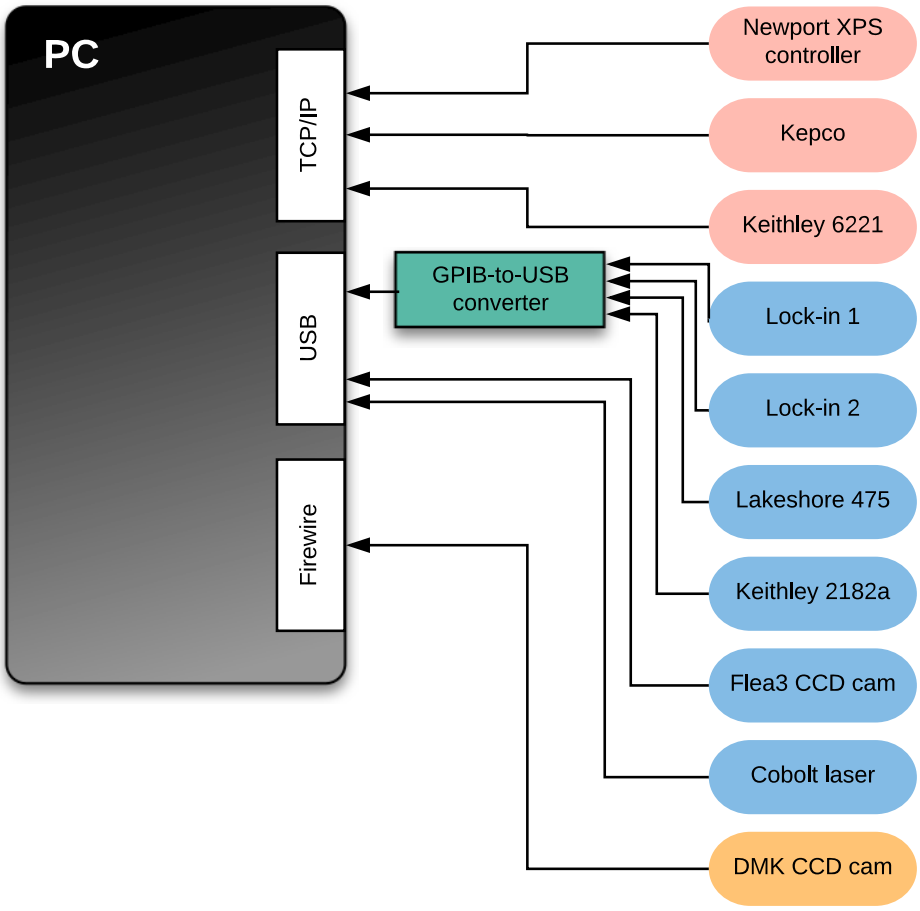

Figure 3.6: Equipment connection map to the PC.

3.2 Optical system

A basic MOKE configuration involves the following key components: a light source, a polarizer, a reflecting sample, an analyzer, and a detector. The design schematic of the optical part of the experimental setup is shown in figure 3.7. The setup can be easily switched to probe the transverse, polar and longitudinal components of the magnetization of magnetic micro- and nanostructures. The configuration chosen on the scope of this work follows the longitudinal MOKE geometry in order to study samples with in-plane magnetization.

This design enabled to perform MOKE measurements while using the heat of the laser to excite magneto-thermal effects on the sample at the same time. Moreover, signal-to-noise ratio is increased by modulating the laser with an optical chooper wheel and using a lock-in detection mechanism, which will be introduced and explained in the next section.

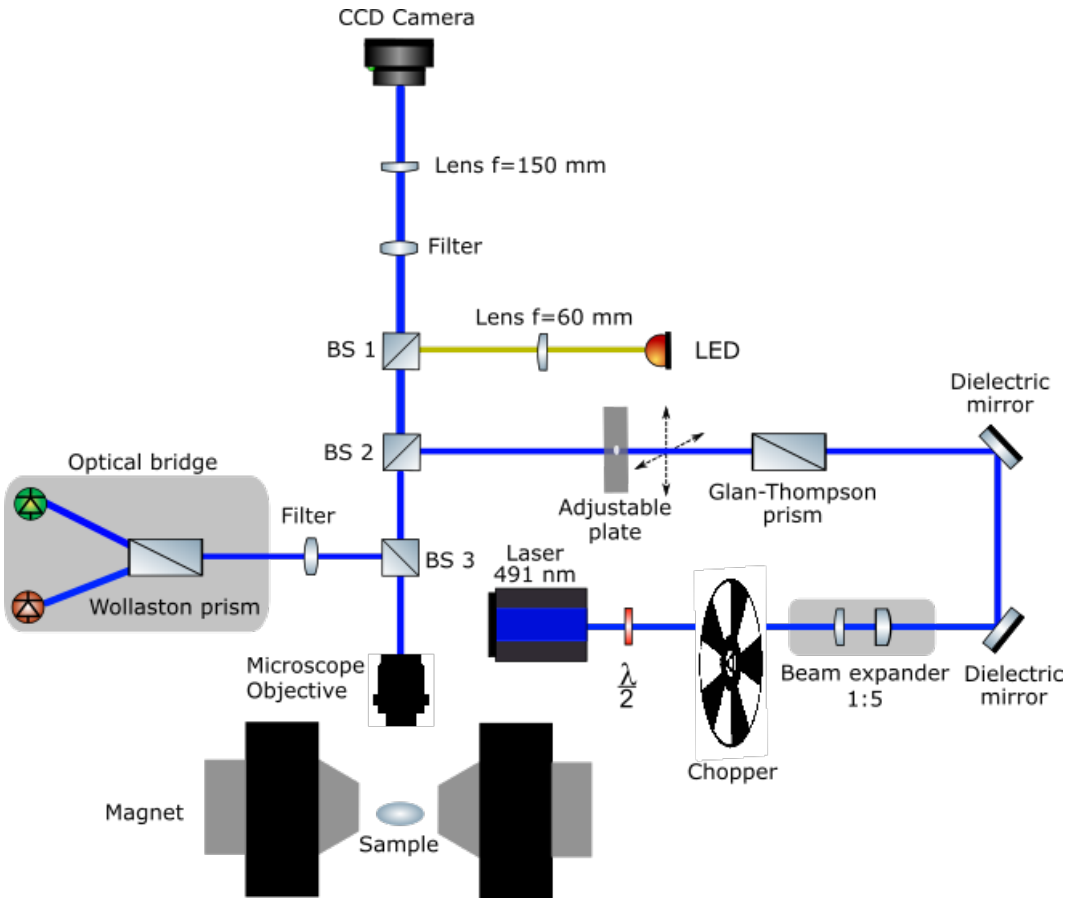

Figure 3.7: Optical part of the experimental setup. BS stands for beam-splitter cube.

The first part of the optical system is the laser source, which was introduced in a previous section. It is a 491 nm wavelength laser, linearly polarized in the vertical direction. Right after the laser source there is a $\lambda/2$ waveplate installed on a rotary

mount which, in conjunction with the first polarizer, serves as an attenuator of the laser. The $\lambda/2$ waveplate induces a rotation of the polarization of the laser light such that the laser light will only partially pass through the first polarizer. In this way, having the $\lambda/2$ waveplate facilitated laser alignment during the installation stage as it could attenuate the laser intensity to safe power levels. The fast axis of the $\lambda/2$ waveplate was measured at 289°, thus meaning the slow axis is at 334°. After the $\lambda/2$ waveplate comes the optical chopper wheel which modulates the laser beam for the lock-in detection technique. The beam expander that follows is a two lense-system that expands the beam diameter on a ratio 1:5. The beam expander has a Keplerian configuration, shown in figure 3.8, in which the focal distance of both lenses despite being different, coincide on the same position. The ratio of focal lengths define the ratio of expansion.

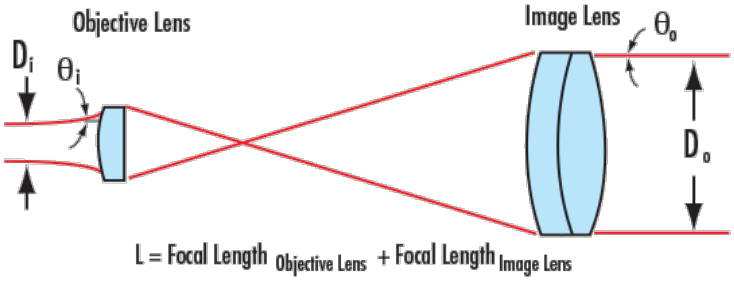

Figure 3.8: Schematic of a Keplerian beam expander. D_i and D_o are the beam input and output diameter respectively. Θ_i and Θ_o are the input and output beam divergence respectively. Taken from [1].

The two broadband dielectric mirrors redirect the laser towards the Glan-Thompson prism which acts as the polarizer. The light comes out being s-polarized with respect to the plane of incidence when it hits the sample. The metallic plate after the Glan-Thompson prism was home-made and contains a mm-sized hole for cutting part of the laser beam and only allowing transmission of a small portion of it. As the plate was designed to be slideable into the tube system, it enabled changing the location of the laser beam so that it could impinge near the edge of the microscope objective aperture, a necessary condition to obtain the incidence angle required for longitudinal MOKE. Figure 3.9 shows the plate.

The beam-splitter cubes were all 50:50 transmission/reflection. This meant that neglecting any loss on the chopper and dielectric mirrors, at most only 25% of the nominal power of the laser will reach the sample. The microscope objective was a Nikon LU Plan with 50x magnification, 0.55 numerical aperture, and a working distance of 10.1 mm. The plane of incidence is parallel to the magnetic field. Figure 3.10 shows the plane of incidence of the s-polarized laser with respect to the sample.

The reflected light beam is collected by the same microscope objective and redirected via BS 3 to the optical bridge. Between the BS 3 and the optical bridge there is a bandpass filter centered at 488 nm to get rid of any collected ambient light and improve the sensibility of the measurement. The optical bridge consists of a

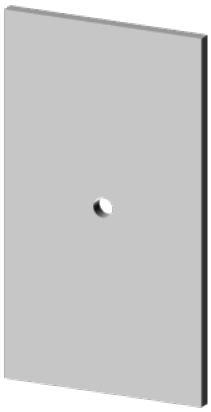

Figure 3.9: Home-made plate to relocate the laser beam for the longitudinal MOKE geometry. The diameter of the hole was 1 mm.

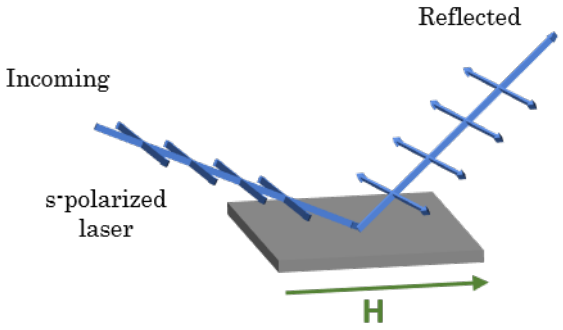

Figure 3.10: Plane of incidence of the s-polarized laser.

Wollaston prism and the Thorlabs PDB210A/M photodetector unit. The Wollaston prism acts as the analyzer and splits the incoming beam into spatially-separated orthogonal components. These orthogonal beams are linearly polarized and are analized by the two photodiodes in the PDB210A/M photodetector unit. This unit substracts both photocurrents from each other, thus reducing the background electric offset making it easier to measure small signals. The optical bridge must be rotated before each measurement until both photocurrents cancel each other. At this orientation both orthogonal components of the light have the same intensity. Whenever the laser beam experiences a polarization rotation due to the Kerr effect, one of these components will be more intense than the other. The difference in intensity translates to difference in the photocurrents, which is proportional to the inflicted rotation. Thus, the differential signal is considered to be proportional to the Kerr angle inflicted on the reflected beam and its relationship is given by

$$\theta_{Kerr} \propto \frac{(I_1 - I_2)}{(I_1 + I_2)} \tag{3.1}$$

Concerning the upper part of the schematic in figure 3.7, the LED source is the

660 nm wavelength Thorlabs model M660L4. It is coupled to the optical system by a collimating lense and a flexible rubber tube that allows tilting of the LED source so lighting can be improved without further modifications to the tubing system. On the way to the CCD camera there is a longpass filter with a 550 nm cut-on wavelength that gets rid of the laser in order to improve the camera image and the pattern recognition algorithms. The last optical element is an achromatic lens with a focal distance of 150 mm that focuses the image into the CCD camera. The CCD camera is a Flea3 monochromatic camera with 1.3 megapixels.

3.3 Signal acquisition

Two sets of signals were needed to be detected: electrical signals picked up from the surface of the sample related to magneto-(thermo)electric effects (Nernst/Magneto-resistance effects) and the MOKE signal coming from the photodetector. These signals have a very low amplitude and as such can be buried in the noise, making it difficult to detect with standard measurement equipment. Therefore, lock-in amplifiers were used for both type of signals.

The lock-in detection schematics for both signals are shown in figures 3.11 and 3.12.

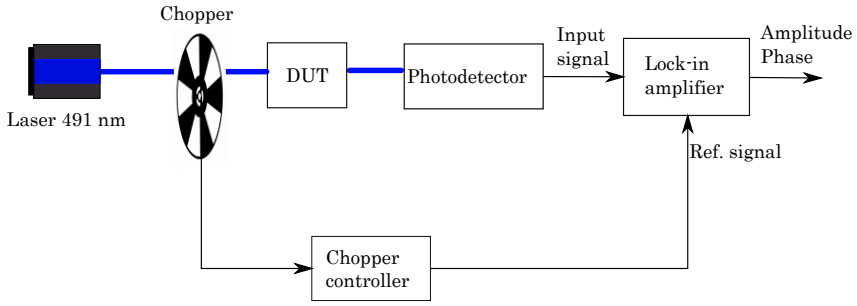

Figure 3.11: Lock-in detection schematic for optical signals. DUT stands for Device Under Test.

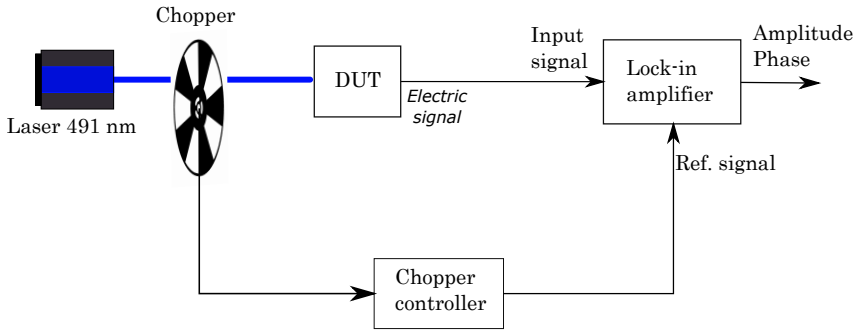

Figure 3.12: Lock-in detection schematic for electric signals. DUT stands for Device Under Test.

In both cases the input signal to the lock-in amplifiers is modulated by the chopper frequency, set by the chopper controller HMS 220. This controller covers frequencies from 0.1 Hz to 10 kHz, depending on the blade used. The chopper frequency is feeded as the reference frequency for the lock-in amplifiers. The electrical signal is picked up by 5 μm diameter tips from Signatone connected with BNC cables to the channels A and B on the lock-in amplifier, which is set in differential mode for better accuracy. Up to 4 DC tips can be installed, enabling 4-point resistance measurements. The tips can be manipulated individually through the XYZ micrometer stages, allowing flexible contacting positions. An additional Nanovoltmeter model Keithley 2182a is installed for applications that do not allow for signal modulation.

3.4 Spatial resolution

The spatial resolution of the setup is limited by the wavelength of the beam and the numerical aperture of the microscope objective [24]. These two factors influence the diffraction pattern of the field at the focal plane of the microscope objective. This diffraction pattern, due to the rotational symmetry of the aperture, has the form of Airy disks, shown in figure 3.13a. The intensity distribution of these disks is shown in figure 3.13b.

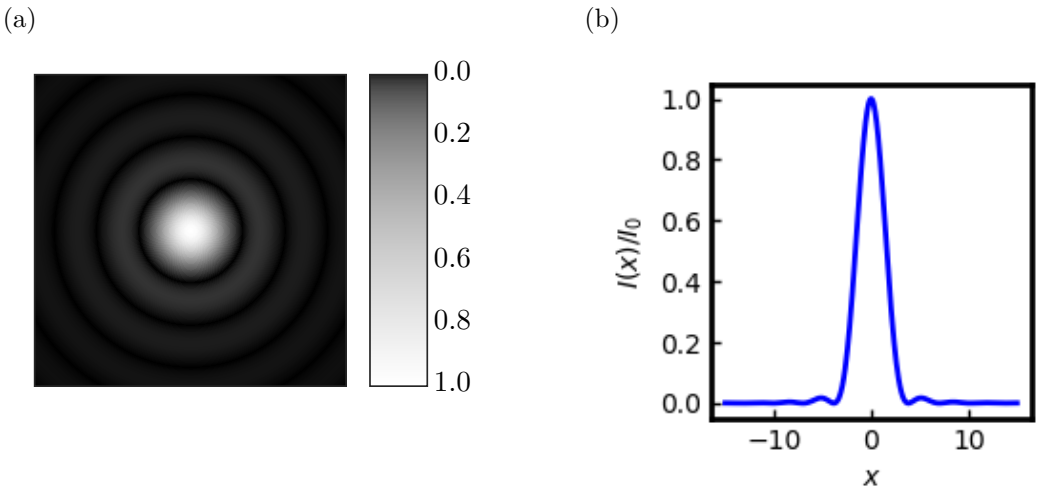

Figure 3.13: (a) Airy disk. Taken from [8]. (b) Intensity distribution of an Airy disk.

The smallest possible diameter of the Airy disk is found by scanning over the z axis and inspecting the diffraction pattern. Figure 3.14 shows the appearance of the Airy disk for a particular sample at $z = -230.71$ μm.

The resolution limit, according to the Rayleigh criterion, is set by equation 3.2 [16]. In this equation, λ is the wavelength of the light and N.A. is the numerical aperture of the microscope objective. This criterion establishes the minimum resolution limit

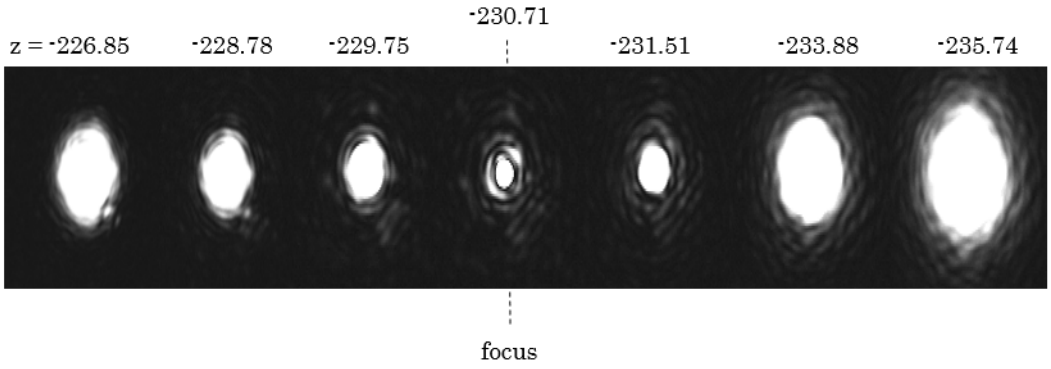

Figure 3.14: Laser intensity at different heights. Shown here is the focus for a particular sample at -230.71 μm.

of the maxima of two Airy curves. The condition is that the maxima of one Airy disk must overlap the minimum of the neighboring disk.

$$r_{\text{Raileigh}} = 0.61\frac{\lambda}{N.A} \tag{3.2}$$

For the setup built, the resolution limit according to Rayleigh's criterion is 544 nm.

3.5 Software

The software used to operate the setup is based on the thaTEC$^{\text{TM}}$software suite. This software is build upon the Labview programming language. The central part of the sofware is the server, named thaTEC:OS, which has the capabilities of coordinating communications and sending instructions to all connected hardware. The experimental process tree is defined in this module, which will then take control of the hardware and run automatically the routine. The UI for the server is shown in figure 3.15.

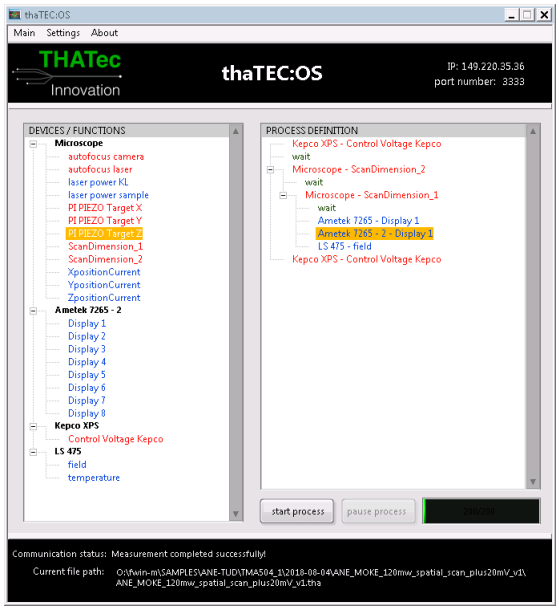

Figure 3.15: thatec:OS server. This module is the central part of the software and controls the communications between all connected hardware.

The magnetic field is controlled by the module Ametek 7265, shown in figure 3.16.

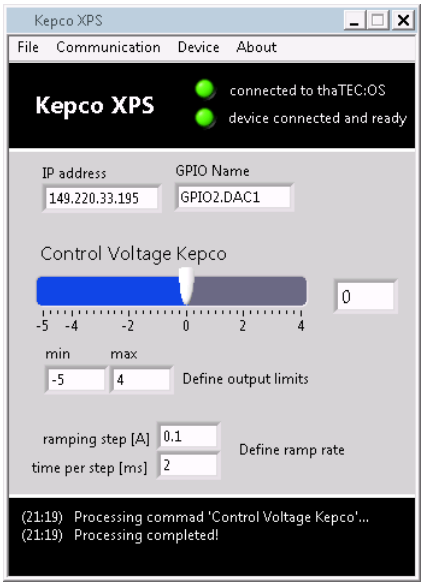

Figure 3.16: Module for controlling the Kepco power supply.

The module to measure the magnetic field is shown in figure 3.17.

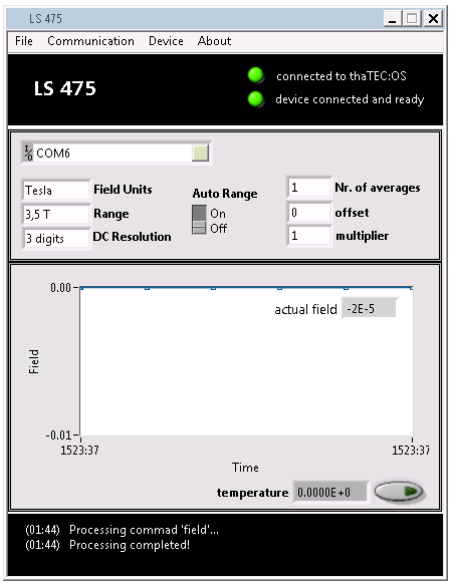

Figure 3.17: Module for controlling the Lake Shore Gaussmeter.

The module for communicating with the lock-in amplifiers is shown in figure 3.18.

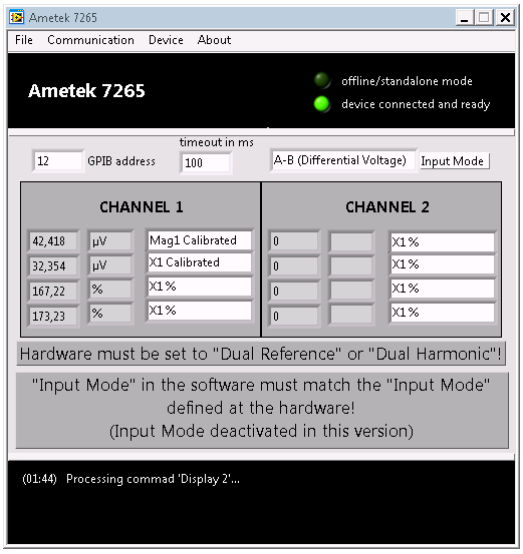

Figure 3.18: Module for controlling the lock-in amplifiers.

The microscope module is shown in figure 3.19.

Figure 3.19: Microscope control software.

The software to control the laser was propietary from Cobolt. Its UI is shown in figure 3.20.

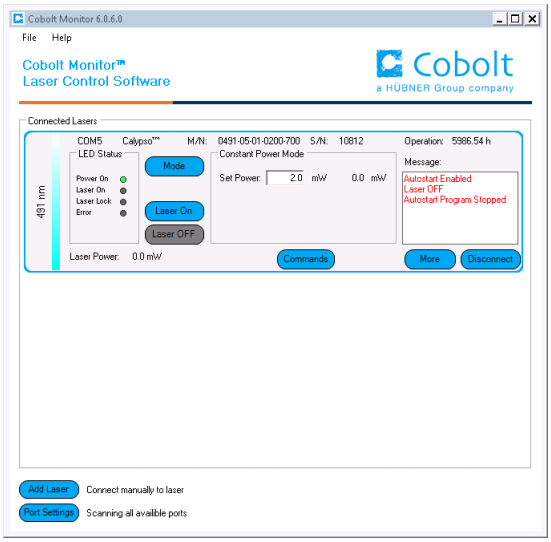

Figure 3.20: Laser control software.

Chapter 4

Applications

This chapter is dedicated to presenting and discussing the experimental results obtained with the setup described in chapter 3. To assess the performance and tune-up its specifications, the setup was used in two different research projects. Differing in complexity, these projects would also help showing the possible working limitations of the laboratory setup and signal the way for future improvements, which are addressed in chapter 5. Furthermore, these projects are interesting research topics on their own and each pose different experimental challenges, which made them even more attractive for initial studying and characterization.

The organization of the chapter is as follows: section 4.1 collects the results of the characterization on Co_2MnGa thin films and in section 4.2 the results on Pt/CoFeB nanowires are presented and discussed.

4.1 Co_2MnGa thin films

Magneto-thermoelectric characterization of thin films of the Weyl semimetal Co_2MnGa were performed, in collaboration with the Institut für Festkörper- und Materialphysik from the Technische Universität Dresden. Additionally, the magneto-optical response of the material was also studied and analyzed.

4.1.1 Motivation

The material Co_2MnGa was reported in 2017 as an experimental candidate towards the study of topological Weyl semimetals [6]. These type of materials are believed to have exotic transport and optical properties due to the nontrivial topology of the band structure [30]. Furthermore, a high anomalous Nernst coefficient was already reported in thin films of this material [30]. Despite this, not much have been reported on the electrical properties of this material and there is still debate around the causes of the large Hall and Nernst conductivities [23]. Therefore, the goal of this project was to investigate the spin-caloritronic and optical behavior of this novel material. Moreover, it would be an ideal scenario to test the setup's simultaneous magneto-optical and magneto-thermal characterization capabilities.

4.1.2 Sample

The sample under study was provided by the Institut für Festkörper- und Materialphysik from the Technische Universität Dresden. The material stack can be seen in 4.1a. The Co_2MnGa films were grown by magnetron sputtering at the Max Planck Institute for Chemical Physics of Solids in Dresden. Afterwards, the Co_2MnGa layer was patterned by optical lithography into Hall bar structures, which are shown in figure 4.1b. The vertical and horizontal stripes are 45 μm and 20 μm width respectively. The horizontal length is roughly 1.8 mm and vertical length 1.3 mm. The contact pads are 200 μm x 150 μm.

(a)

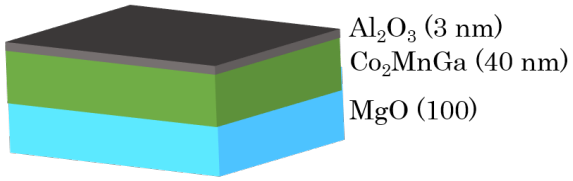

(b)

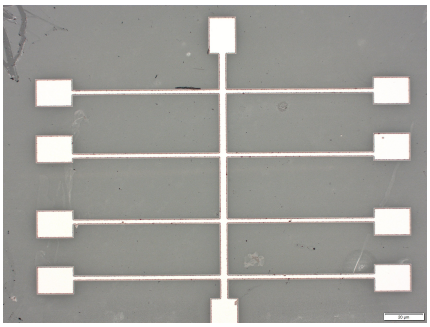

Figure 4.1: (a) Material stack. (b) Overview of the Hall bars in an optical microscope. Courtesy of Helena Reichlova (TU Dresden).

4.1.3 Results

Magneto-transport characterization

Anisotropic magnetoresistance measurements were performed on the sample. The experiment design followed a planar Hall effect geometry, which is shown in figure 4.2. In this type of experiment, the external magnetic field lies in the same plane as the electric field and the transverse Hall voltage that arises, called Planar Hall Voltage (V_{xx} in the figure). In Weyl semimetals, the Planar Hall Effect is described as in equation 4.1 [22]. Equation 4.2 denotes the longitudinal resistivity, ρ_{yy}. $\rho_\perp$ is the resistivity when the electric field and the magnetization are perpendicular, and $\rho_\parallel$ when they are parallel.

$$\rho^{PHE} = -(\rho_\perp - \rho_\parallel)\sin\theta\cos\theta \tag{4.1}$$

$$\rho_{yy} = \rho_\perp - (\rho_\perp - \rho_\parallel)\cos^2\theta \tag{4.2}$$

To perform the PHE measurements a Keithley Nanovoltmeter model 2182a and a Keithley Current Source model 6221 were used. The DC current applied was 200

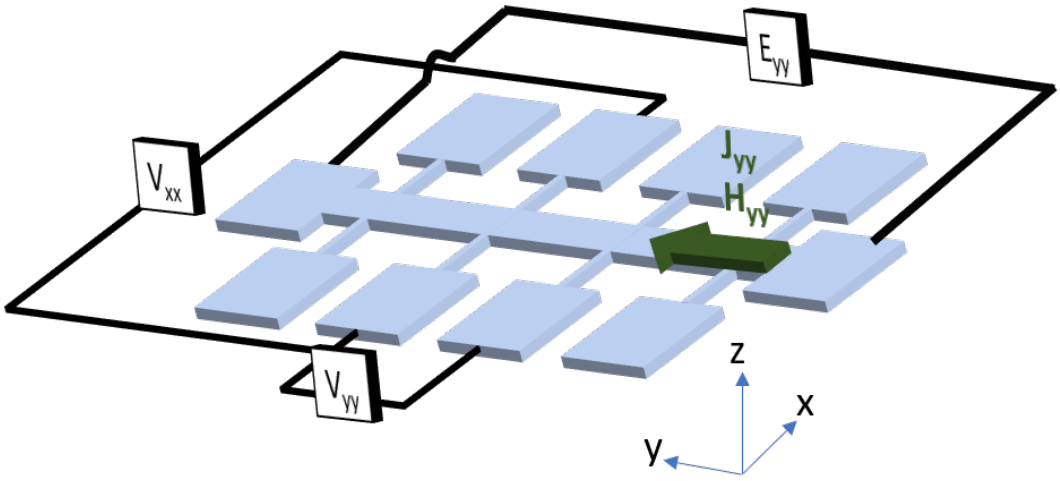

Figure 4.2: Measurement schematic for the magneto-transport characterization.

μA and the magnetic field direction was along the current direction. Signatone 5 μm probe tips were used for the current injection and voltage detection.

The magnetoresistance response is captured in figure 4.3. Figure 4.3a shows the change in the longitudinal resistance R_{yy} while figure 4.3b shows the change in the transverse resistance R_{xx}.

(a) (b)

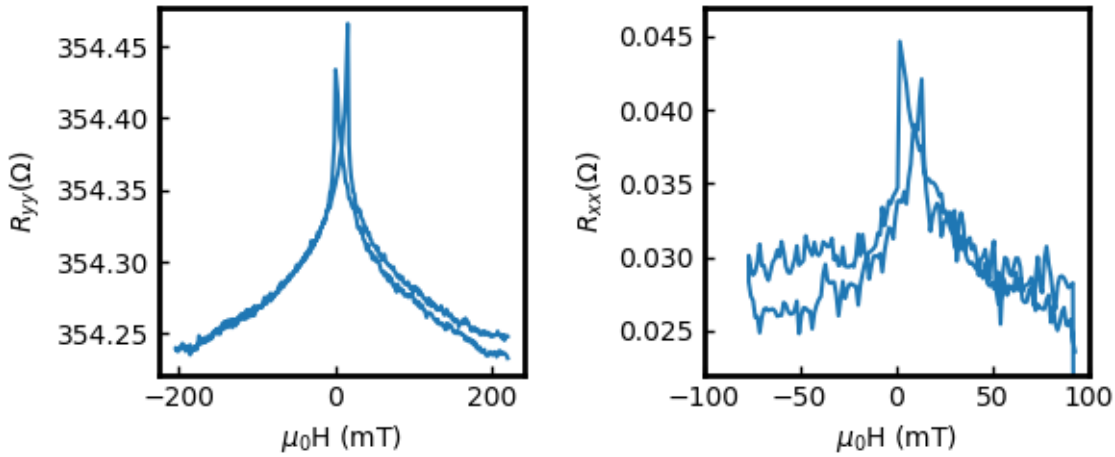

Figure 4.3: (a) Longitudinal AMR. (b) Transverse AMR.

The negative (lower) magnetoresistance shown at saturation in both the longitudinal and transverse directions as seen in figure 4.3 has been predicted by several groups as a distinctive signature of Weyl semimetals [22, 39]. This effect is stronger

when $B \parallel E$, contrary to what is seen in classical positive magnetoresistance in normal magnetic metals. The causes of this phenomenon are still under debate. Chiral anomaly, that is, the violation of the conservation of chiral charges under the presence of parallel electric and magnetic fields, is being believed as the primary source of this negative magnetoresistance [26]. A chiral charge is any charge that can have its spin either parallel or antiparallel to its direction of motion. It can also be understood as the different directions of the projection of the spin vector onto its momentum vector [37]. An example for chiral charges arises in the quantum field theory where massless fermions segregate into left-handed and right-handed chiral groups [38]. In the context of Weyl semimetals, the chiral charges are the Weyl fermions, which are split into separated Dirac cones. Under the conservation of chiral charges, these separated chiral populations should not mix. However, when an electric and magnetic field are applied parallel to each other, they can push Weyl fermions from one Weyl node (the point in momentum space where the Dirac cones touch) to another of opposite chirality, since Weyl nodes are separated just in momentum space [18]. This violates the conservation of chiral charges and creates an axial charge current, making the Weyl semimetal more conductive in parallel electric and magnetic fields. The chiral anomaly phenomenon is iluustrated in figure 4.4.

(a) (b)

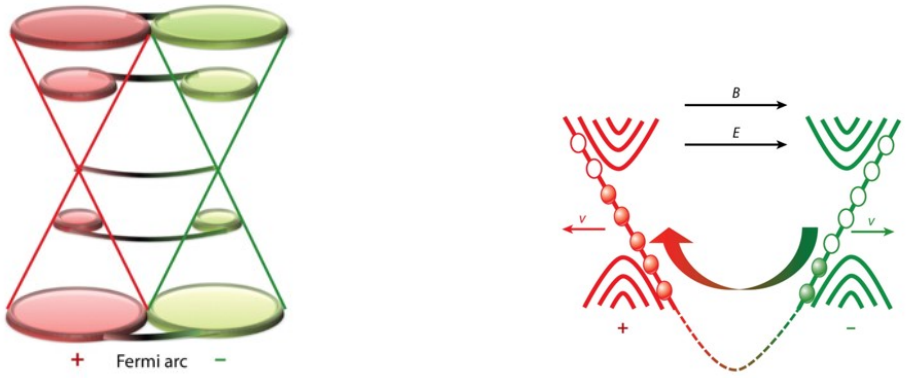

Figure 4.4: Chiral anomaly in Weyl semimetals. Taken from [39]. (a) Spatially separated Dirac cones with opposite chirality connected by Fermi arcs. (b) Under the application of parallel electric and magnetic fields Weyl fermions will travel with opposite velocities due to different chirality and an imbalance in the densities of chiral charges will appear.

Another possible contribution to the negative magnetoresistance is the suppression of back-scattering between Weyl fermions of opposite chirality improving the conductivity in the material [27, 34]. Furthermore, other research groups have pointed towards the 'current-jetting' effect, which is a highly non-uniform current distribution inside the sample which yields a distortion in the potential, as the cause of the negative magnetoresistance [10]. The positive magnetoresistance seen in the neighborhood of 0 mT can be understood as a result of increased scattering processes

due to the appearance of a Lorentz force when $B \perp E$ [39].

Magneto-optical characterization

The optical properties of Co_2MnGa have not been extensively reported so far [30]. For this reason, longitudinal magneto-optical Kerr effect measurements were performed on the sample.

Figure 4.5 shows the magnetic response of the material obtained from the L-MOKE experiments. The inset of the figure shows the location of the laser spot and the direction of the magnetic field. The plane of incidence of the laser is normal to the surface of the sample and parallel to the magnetic field.

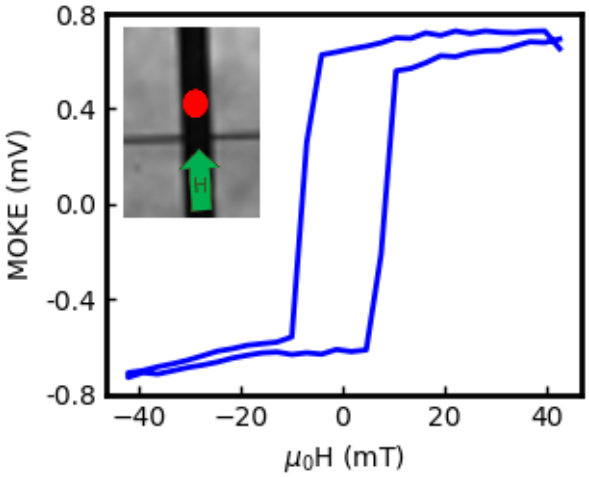

Figure 4.5: Magnetic hysteresis curve from MOKE measurements.

The hysteresis curve from figure 4.5 shows a sharp hysteretic switch with a coercive field value of 8.49 mT. This type of material was reported to show perpendicular magnetic anisotropy in thin films, showing that in the form of nanowires shape anisotropy might be a dominating term [15]. Further magnetometry measurements must be done to derive further conclusions.

The energy density, E_D, was calculated using $E_D = M_S \times H_C$, where M_S is the saturation magnetization and H_C is the coercive field. Using 700 kA/m as saturation magnetization taken from [30] and a coercive field of 8.49 mT, E_D results in 5.9 kJ/m^3 which is in a similar range to the 10 kJ/m^3 value reported for $Mn_{2.6}Co_{0.3}Ga_{1.1}$ in [15]. In this work they expected that further addition of Co would reduce more the energy density.

Using the same L-MOKE technique, spatial maps were performed on one of the crosses of the Hall bar in order to get insights on magnetic microstructures, grains, and domain wall formation. For this, the laser was focused on the sample and scanned in steps of 4.56 μm in x and 2.88 μm in y. The photodetector unit was rotated so that before starting the measurement the difference in the signal from the

two photodiodes was approximately 0 mV, thus increasing the sensitivity. Figure 4.6a shows the spatial maps obtained at magnetic field values for saturation and close to zero field. The green arrow inside the maps shows the direction of the magnetic field. The orientation of the sample and the location of the scanning region is shown in figure 4.6b.

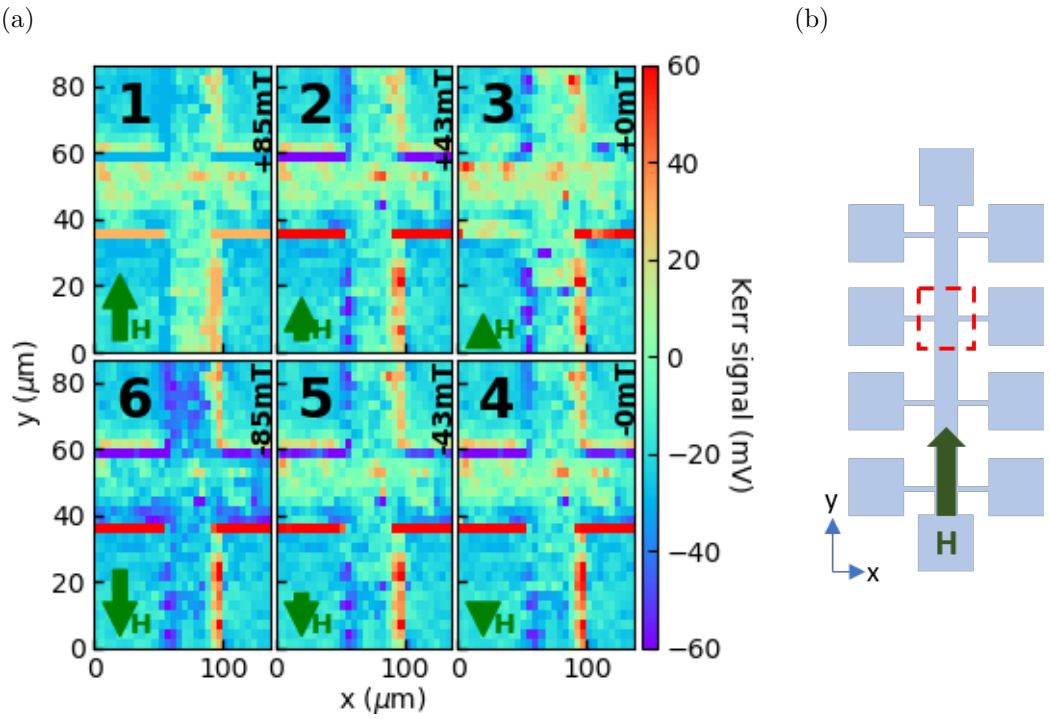

Figure 4.6: (a) Spatially-resolved MOKE maps. Opposite magnetization states are evidenced by the contrast of the Kerr signal. The length of the small green arrow at the bottom left corner of the maps represents the intensity and orientation of the magnetic field. The order in which the magnetic field was applied is indicated by the number in the top-right corner of each map. (b) The 137 μm × 86 μm scanning region of the Hall bar is enclosed in the red-dashed lines. Also shown is the direction of the field.

The μV signal in figure 4.6a is proportional to the Kerr angle as stated in equation 3.1. As such it can be seen that non-magnetic material shows a signal near 0 V which corresponds to almost no Kerr effect at all as expected. This explains the green color of the substrate. The signal with a magnetic origin shows in orange/red and blue/purple, according to opposite ends of the saturation magnetization.

It must be noted that this scanning MOKE technique is surface sensitive and, as such, any surface roughness or microstructure edge can destroy the Kerr signal. At these surface inhomogeneities the polarization state of the light is destroyed which in turn eliminates the direct relationship between the photocurrent and the Kerr angle. This can be seen on figure 4.6a as the peaks coming from the borders of the

structure, which derive no magnetic meaning. The consistent peaks in the center of the cross also denotes the possible existence of a surface inhomogeneity that is distorting the Kerr signal.

Magneto-thermoelectric characterization

Magneto-thermoelectric characterization by accounts of the anomalous Nernst effect was done on Co_2MnGa. The schematic of the experiment is shown in figure 4.7. This experimental geometry consists in having a laser-induced out-of-plane thermal gradient ∇T perpendicular to the magnetization **M** of the material, as denoted in formula 2.11. Therefore, the external magnetic field **H** was set in the plane of the sample, perpendicular to the thermal gradient. V_{ANE} is the transverse voltage that arises due to the anomalous Nernst effect. The coordinate system shown in figure 4.7 follows the direction of the stages' coordinate system.

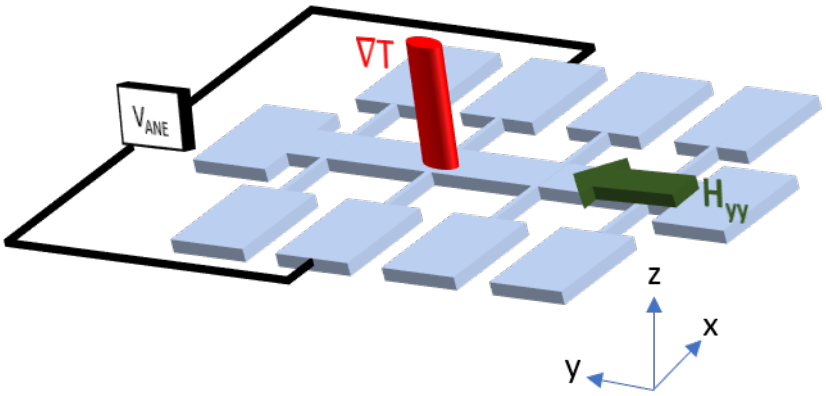

Figure 4.7: Measurement schematic for the magneto-thermoelectric characterization.

First, the transverse anomalous Nernst voltage, V_{ANE}, was measured as a function of $\mu_0 H$. The resulting V(H) hysteresis curve is shown in figure 4.8. The inset part of the figure shows the laser-spot position and the direction of the magnetic field. A sharp hysteretic switch with a coercive field value of 18 mT can be seen. This increased coercive field with respect to the one obtained from figure 4.5 could be due to a more dominating shape anistropy term in one of the thinner *alleys* of the Hall cross.

In order to ellucidate on magnetic microstructures, spatially-resolved mapping of local thermoelectric measurements of the Hall bar were done. Figure 4.9 shows the V_{ANE} as a function of the laser-spot position (x, y). The voltage V_{ANE} is considered to be proportional to E_{ANE} from equation 2.11. Figure 4.9a shows the spatial-resolution of the transverse thermoelectric voltage V_{ANE}. The direction and intensity of the magnetic field is represented by the small arrows. Figure 4.9b shows the orientation of the Hall bar, the scanning area and the location of the laser spot. The laser impinged perpendicularly on the sample, generating a non-uniform thermal gradient that varied with the film thickness. The laser beam transfers part of its energy into

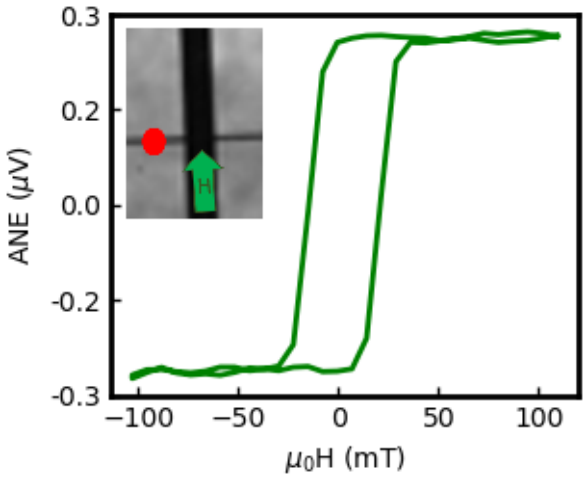

Figure 4.8: Magnetic hysteresis curve from magneto-thermal measurements.

the film, which generates a thermal gradient $\nabla T_z(x, y)$ for every (x,y) position of the laser spot. In-plane components of the thermal gradient are radially symmetrical, hence, cancel out and do not contribute to any magneto-thermal effect [36]. Given that the thermal gradient is hard to quantify, an empirical approach was used. This approach resulted in equation 4.3, where V_{meas} is the measured Nernst voltage, L_{diam} is the laser spot diameter and N_{ANE} is the Nernst coefficient taken as -2 μV/K [30].

$$\frac{V_{\text{meas}}}{L_{\text{diam}} \times N_{\text{ANE}}} = \nabla T_z(x, y) \tag{4.3}$$

Taking L_{diam} as the theoretical value of 544 nm from equation 3.2, the resulting ∇T is of 0.3 K/μm.

For the maps in figure 4.9a, the laser was focused on the sample and scanned in steps of 4.56 μm on x and 2.88 μm on y. At ±85mT there are no magnetic microstructures visible as the sample is in saturation. The recorded V_{ANE} for +85 mT is of roughly 2.3 μV. The vertical part of the cross shows no signal because at these locations both electrical contacts are at the same electrical potential, thus experiencing no net thermoelectric voltage. The area exactly in the middle of the cross is showing less anomalous Nernst voltage probably due to shunting effects. Given that in this position the laser spot is surrounded by more conductive material, an electrical current will appear in the surrounding area of $\nabla T_z(x, y)$ thus decreasing the V_{ANE}. This shunting effect is illustrated in figure 4.10. As the magnetic field is reduced the signal becomes weaker and at -7 mT the first microstructures appear. Three magnetic domains begin to appear, two of them nucleating first at the extremes of the nanowire and one remaining in the central part (show in red at -7 mT). As the magnetic field continues to be decreased, the domains fuse and turn into a single domain. The sign reversal of V_{ANE} along the reversal of the field clearly indicates

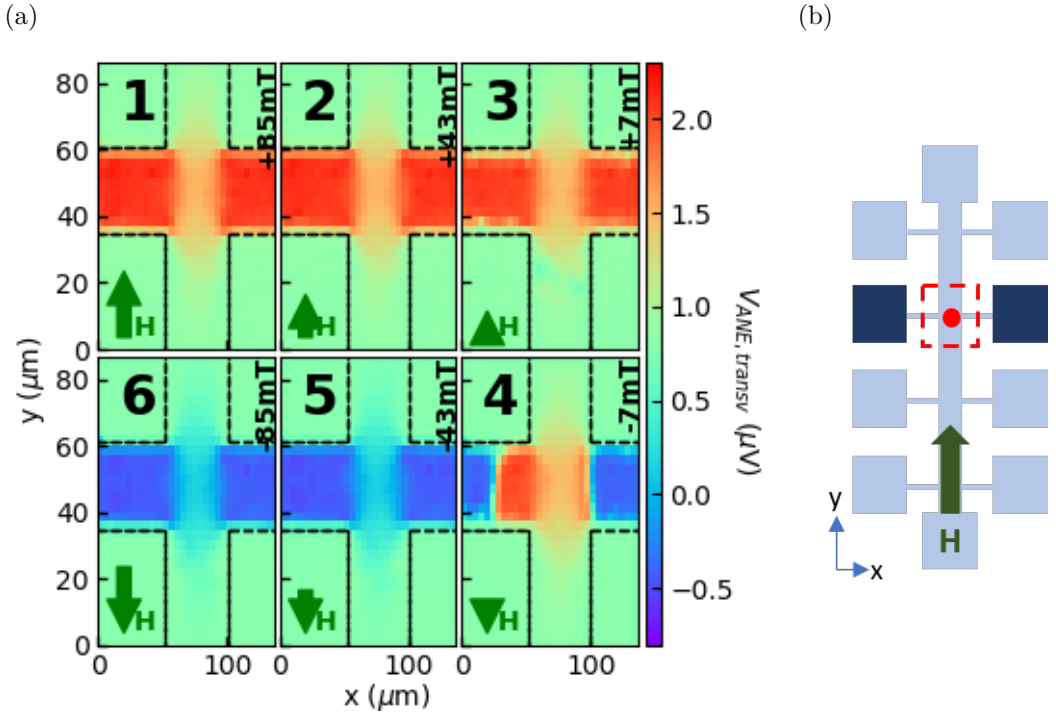

Figure 4.9: (a) Spatially-resolved transverse ANE maps. The dc voltage V_{ANE} arises due to the anomalous Nernst effect. When reversing the field, magnetic microstructures start to appear. Dashed lines define the boundaries of the Hall cross. The length of the small green arrow at the bottom left corner of the maps represents the intensity and orientation of the magnetic field. The order in which the magnetic field was applied is indicated by the number in the top-right corner of each map. (b) The 137 μm $\times$ 86 μm scanning region of the Hall bar is enclosed in the red-dashed lines. The contact pads used to pick up the thermoelectric voltage are highlighted in dark blue. Also shown is the direction of the field and the laser-spot location (the red dot).

that it comes from the cross-product term $\mathbf{M} \times \nabla T$, ruling out any field-symmetric thermopower effect as the possible cause.

A spatially-resolved mapping of the local magneto-thermoelectric effects in the longitudinal orientation is shown in figure 4.11a. The aim of this experiment is to segregate the contributions from the anomalous Nernst effect and the anisotropic magneto-thermopower. For this, the laser was focused on the sample and scanned in steps of 2.74 μm on x and 8.72 μm on y. In the center, wider part of the cross there is no signal due to the possibilities of the signal being completely shunt or due to a low AMT coefficient which would decrease the in-plane thermal conduction. More experiments are needed to be able to derive further conclusions. The signal reversal in the thinner left *alleys* of the Hall cross is simply due to just probing one side of the anomalous Nernst effect. While the laser is in the top left alley, one contact pad

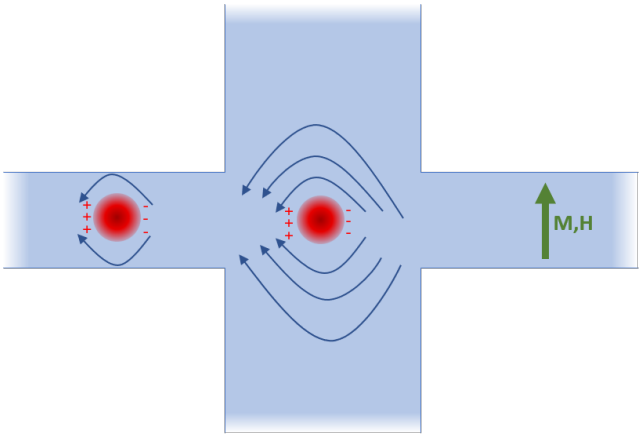

Figure 4.10: Local shunting effects. When the laser-spot is in the center of the cross, it is surrounded by more conductive material than in the thinner *alleys* located on the sides. The access to more conductive material provides a lower resistance path for charge carriers, which translates into the appearance of a local charge current surrounding the area of the thermal gradient. This reduces the ANE effect experienced on this location. With the laser-spot located in the left *alley* the shunting effects are minimized given that there is less metal surrounding the thermal gradient.

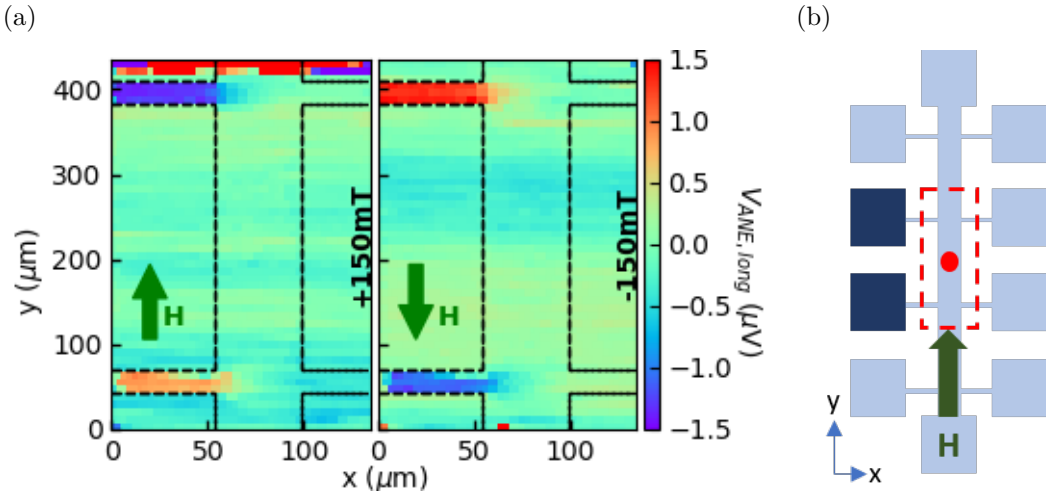

Figure 4.11: (a) Spatially-resolved longitudinal ANE maps. The dc voltage $V_{\mathrm{ANE,long}}$ arises due to the anomalous Nernst effect. Dashed lines define the boundaries of the Hall cross. The green arrow inside the maps represents the intensity and orientation of the magnetic field. (b) The 137 μm $\times$ 436.2 μm scanning region of the Hall bar is enclosed in the red-dashed lines. The contact pads used to pick up the thermoelectric voltage are highlighted in dark blue. Also shown is the direction of the field and the laser-spot location (the red dot).

will show HI signal while the other one will have LO signal. When the laser is in the bottom left alley and without doing any recontacting, the voltage and current will just reverse.

4.2 Pt/CoFeB nanowires for spin-Hall nano-oscillators

Spatially-resolved reflectivity maps were done on Pt/CoFeB nanowires as a first step in a research project to investigate domain-wall based spin-Hall nano-oscillators. The motivation, sample information, results, and outlook are presented in the following sections.

4.2.1 Motivation

Spin-Hall oscillators based on nanoconstrictions have already been reported [9, 11]. However, these geometries are static and inflexible, which renders them ineffective for possible applications in neuromorphic computing and dynamic microwave circuits. Thus, scientists have been looking for other more suitable magnetic textures which could fill the requirements. The goal of this project is to investigate domain walls as a candidate structure for spin-Hall oscillators. Domain walls have already been proven as nano-channels for spin-waves [35]. Furthermore, back in 2008 a novel concept of memory device involving current-induced domain wall motion was reported by Parkin et. al [28]. Given its size, dynamic nature and controlability, domain walls could represent a possible way of creating a reprogrammable and flexible solution for nano-sized spin-Hall oscillators.

4.2.2 Sample

The material stack used is shown in figure 4.12. The films were deposited by magnetron sputtering and were patterned by electron beam lithography into nanowires of 100 nm, 200 nm, 300 nm, 400 nm, and 500 nm wide. The nanowires used in this work are shown in figure 4.13.

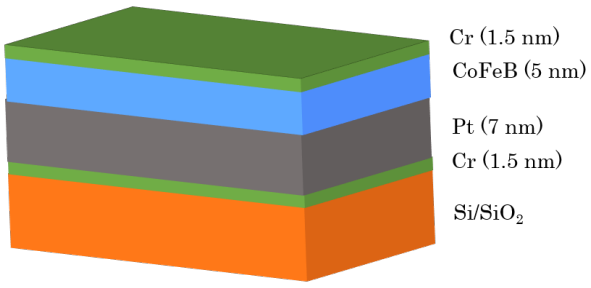

Figure 4.12: Material stack for the domain wall spin-Hall nano-oscillators.

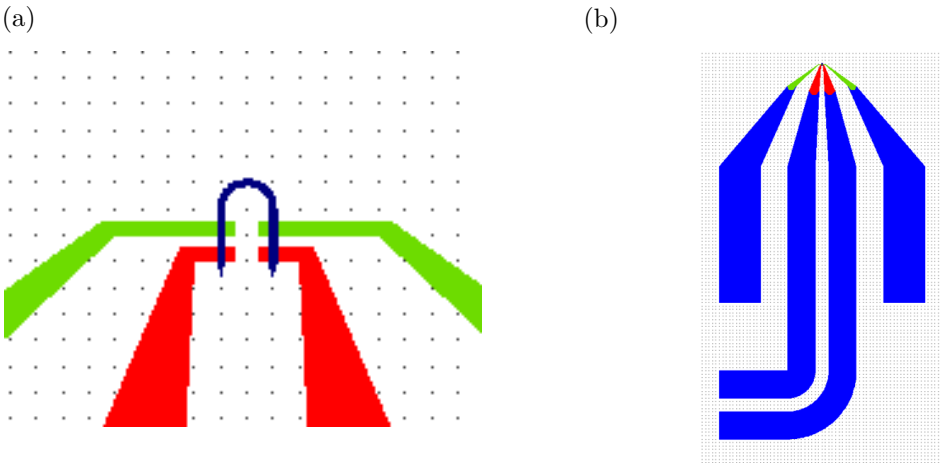

Figure 4.13: (a) Close-up view of a 300 nm wide Pt/CoFeB nanowire (b) Nanowire with the contact pads

4.2.3 Results

The spatially-resolved reflectivity map of the Pt/CoFeB nanowire is shown in figure 4.14. The laser was focused on the sample and scanned in steps of 0.14 μm in x and 0.0577 μm in y. The figure shows that the nanowire can be clearly identified and distinguished from the contacts with the electrical pads and the substrate.

For this measurement the photodetector unit was rotated in order to align the optical axis of the Wollaston prism along the polarization axis of the reflected light beam, so that there is no separation into perpendicular components of the light. In this way a greater sensitivity of the measurement was ensured.

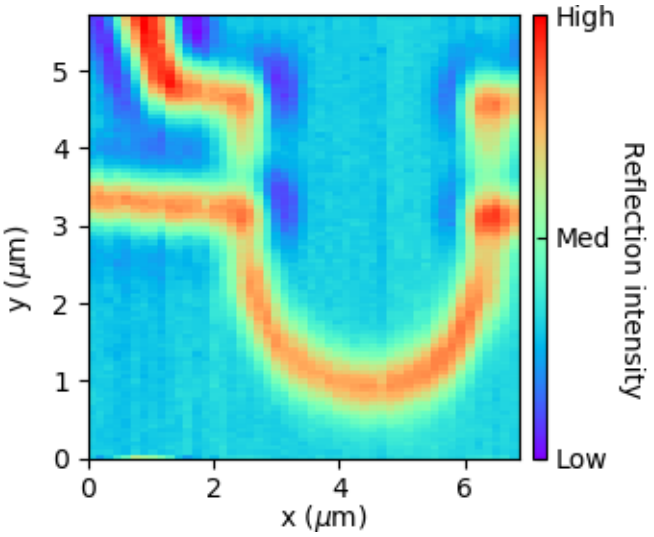

Figure 4.14: Reflectivity map for the Pt/CoFeB nanowire.

Chapter 5

Conclusions and future work

An experimental tool for the study of magnetic spin textures in magnetic hybrid nanostructures was built. This tool is based upon the MOKE effect and characterizes the magneto-optical and magneto-thermoelectric properties of nanostructures in a fast, reliable, and non-invasive way. Through a nano-precision positioning system and a diffraction-limited spatial resolution of 544 nm, it can provide insights into the magnetic textures and dynamics in many challenging scenarios. Furthermore, its capacity for 4 DC probes and 2 microwave picoprobes allows maximum measurement flexibility. Low signal-to-noise ratio was achieved due to the inclusion of lock-in detection schemes. The setup was tested on two application settings and succesfully helped to study the magneto-thermoelectric properties of the Weyl semimetal Co_2MnGa. An important challenge encountered was achieving simultaneous magneto-optical and magneto-thermal measurements on a sample. To achieve a MOKE measurement the home-made plate with the mm-sized hole was necessary, however, this cut most of the laser power needed to induce a thermal gradient for the anomalous Nernst experiment. Choosing not to use the plate made doing longitudinal MOKE not possible. The solution was found by creating a new type of plate with different geometry of the hole such that this satisfied both experimental requirements. A pending work is to continue with the research project to investigate magnetic spin textures for spin-Hall nano-oscillators in Pt/CoFeB nanowires. This will probably be done by the author during his future PhD studies. Also the anomalous Nernst effect will be investigated in antiferromagnetic materials.

Despite being a working and functional setup that has delivered results, it is not a finished product and can always improve. The following actions comprise an upgrade plan that attempts to enhance the setup operation, range of applications, and overall performance:

i Automate the calibration of the optical bridge through a motorized rotation stage and a servo-controller. This would save preparation time before each measurement and enable longer and successive experiments, thus achieving a higher level of automation.

ii Create a Labview module for the control of the Cobolt Laser. This would

enable automated control from the thaTEC:OS server software thus making it possible to dynamically change the laser parameters in runtime.

iii Calculate laser beam width at sample with the Knife Edge method.

iv Due to the interchangeability of the DC probes connections (to the lock-in amplifiers or the nanovoltmeter or the current source), build an intermediate connection box to avoid direct handling of the needles, thus enhancing their lifetime.

Acknowledgements

My professional life has given a 180°change in the last two years and there are many people I have to thank for this. First of all, my parents and my brothers, for constantly pushing me to pursue higher challenges and convincing me to go for a master degree. It was one of the best decisions of my life and simply put, without them I would not be here. I would also like to thank Dr. Helmut Schultheiss for his guidance and supervision for the past 10 months. I started knowing nothing about experimental physics and through your constant support I can safely say I am a more capable researcher now. I want to also thank all the Magnonics group at Helmholtz Zentrum Dresden-Rossendorf for the great work environment and for simply being amazing people. Special thanks to Tobias Hula and Lukas Ehm who both helped me a lot during the course of my thesis. Finally, I want to thank Dr. Helena Reichlova for the opportunity to work on the anomalous Nernst effect project which resulted in many fruitful discussions and learning experiences.

Statement of authorship

I hereby certify that I have authored this Master Thesis entitled "Construction of a measurement instrument for magneto-optical and magneto-thermoelectric characterization of magnetic spin textures in micro- and nanostructures" independently and without undue assistance from third parties. No other than the resources and references indicated in this thesis have been used. I have marked both literal and accordingly adopted quotations as such. There were no additional persons involved in the intellectual preparation of the present thesis. I am aware that violations of this declaration may lead to subsequent withdrawal of the degree.

Dresden, 20.09.2018

Mauricio José Bejarano Rodríguez

Bibliography

[1] Beam Expanders | Edmund Optics. [Online; Accessed: 2018-09-10].

[2] M. Ali. *Growth and study of magnetostrictive FeSiBC thin films for device applications*. PhD thesis, 1999. Bibliographic information available from INIS: http://inis.iaea.org/search/search.aspx?orig_q=RN:31036409; Available from British Library Document Supply Centre- DSC:DXN032443.

[3] L. Berger. Side-jump mechanism for the hall effect of ferromagnets. *Phys. Rev. B*, 2:4559–4566, Dec 1970.

[4] J. A. C. Bland, M. J. Padgett, K. D. Mackay, and A. D. Johnson. Investigation of the magnetic properties of sandwiched epitaxial fe and co films using the magneto-optic kerr effect. *Journal of Physics: Condensed Matter*, 1(27):4407, 1989.

[5] S. R. Boona, R. C. Myers, and J. P. Heremans. Spin caloritronics. *Energy Environ. Sci.*, 7:885–910, 2014.

[6] G. Chang, S.-Y. Xu, X. Zhou, S.-M. Huang, B. Singh, B. Wang, I. Belopolski, J. Yin, S. Zhang, A. Bansil, H. Lin, and M. Z. Hasan. Topological hopf and chain link semimetal states and their application to co_2mnga. *Phys. Rev. Lett.*, 119:156401, Oct 2017.

[7] J. L. Cheng and M. W. Wu. Kinetic investigation of the extrinsic spin hall effect induced by skew scattering. *Journal of Physics: Condensed Matter*, 20(8):085209, 2008.

[8] W. Commons. File:airy-pattern.svg — wikimedia commons, the free media repository, 2017. [Online; accessed 13-September-2018].

[9] B. Divinskiy, V. E. Demidov, A. Kozhanov, A. Rinkevich, S. Demokritov, and S. Urazhdin. Nanoconstriction spin-hall oscillator with perpendicular magnetic anisotropy. 111, 06 2017.

[10] R. D. dos Reis, M. O. Ajeesh, N. Kumar, F. Arnold, C. Shekhar, M. Naumann, M. Schmidt, M. Nicklas, and E. Hassinger. On the search for the chiral anomaly in weyl semimetals: the negative longitudinal magnetoresistance. *New Journal of Physics*, 18(8):085006, 2016.

[11] P. Durrenfeld, A. A. Awad, A. Houshang, R. K. Dumas, and J. Akerman. A 20 nm spin hall nano-oscillator. *Nanoscale*, 9:1285–1291, 2017.

[12] H. E. Edens. Construction and characterization of a magneto-optical kerr effect instrument for studies of ferrimagnetic gdfe films. Master's thesis, University of Amsterdam, 4 2002.

[13] E. Fermi. *Nuclear physics: a course given by Enrico Fermi at the Univ. of Chicago*. Univ. of Chicago Press, 1950.

[14] A. Fert. Two-current conduction in ferromagnetic metals and spin wave-electron collisions. *Journal of Physics C: Solid State Physics*, 2(10):1784, 1969.

[15] C. Fowley, S. Ouardi, T. Kubota, O. Yildirim, A. Neudert, K. Lenz, V. Sluka, J. Lindner, J. M. Law, S. Mizukami, G. H. Fecher, C. Felser, and A. M. Deac. Direct measurement of the magnetic anisotropy field in Mn-Ga and Mn-Co-Ga Heusler films. *Journal of Physics D Applied Physics*, 48(16):164006, Apr. 2015.

[16] L. R. F.R.S. Xxxi. investigations in optics, with special reference to the spectroscope. *The London, Edinburgh, and Dublin Philosophical Magazine and Journal of Science*, 8(49):261–274, 1879.

[17] B. Hillebrands, K. Ounadjela, and Editors. *Spin dynamics in confined magnetic structures I*. Springer, 2002.

[18] S. Jia, S.-Y. Xu, and M. Z. Hasan. Weyl semimetals, fermi arcs and chiral anomalies. *Nature Materials*, 15:1140 EP –, Oct 2016.

[19] S. Joachim and H. C. Siegmann. *Magnetism: from fundamentals to nanoscale dynamics*. Springer, 2006.

[20] R. Karplus and J. M. Luttinger. Hall effect in ferromagnetics. *Phys. Rev.*, 95:1154–1160, Sep 1954.

[21] W. Kleemann. *Magneto-optical Materials*. American Cancer Society, 2007.

[22] N. Kumar, S. N. Guin, C. Felser, and C. Shekhar. Planar Hall effect in the Weyl semimetal GdPtBi. *Physical Review B.*, 98(4):041103, July 2018.

[23] Y. Kurtulus, R. Dronskowski, G. D. Samolyuk, and V. P. Antropov. Electronic structure and magnetic exchange coupling in ferromagnetic full heusler alloys. *Phys. Rev. B*, 71:014425, Jan 2005.

[24] J. Li. *A scanning Kerr microscope with high spatial and temporal resolutions*. PhD thesis, Universitat Bochum, 2010.

[25] N. F. Mott. The electrical conductivity of transition metals. *Proceedings of the Royal Society of London A: Mathematical, Physical and Engineering Sciences*, 153(880):699–717, 1936.

[26] S. Nandy, G. Sharma, A. Taraphder, and S. Tewari. Chiral anomaly as the origin of the planar hall effect in weyl semimetals. *Phys. Rev. Lett.*, 119:176804, Oct 2017.

[27] H. B. Nielsen and M. Ninomiya. The Adler-Bell-Jackiw anomaly and Weyl fermions in a crystal. *Physics Letters B*, 130:389–396, Nov. 1983.

[28] S. S. P. Parkin, M. Hayashi, and L. Thomas. Magnetic domain-wall racetrack memory. *Science*, 320(5873):190–194, 2008.

[29] S. Polisetty, J. Scheffler, S. Sahoo, Y. Wang, T. Mukherjee, X. He, and C. Binek. Optimization of magneto-optical kerr setup: Analyzing experimental assemblies using jones matrix formalism. 79:055107, 06 2008.

[30] H. Reichlova, R. Schlitz, S. Beckert, P. Swekis, A. Markou, Y.-C. Chen, S. Fabretti, G. H. Park, A. Niemann, S. Sudheendra, A. Thomas, K. Nielsch, C. Felser, and S. T. B. Goennenwein. Large anomalous Nernst effect in thin films of the Weyl semimetal Co2MnGa. *ArXiv e-prints*, July 2018.

[31] O. Reimer, D. Meier, M. Bovender, L. Helmich, J.-O. Dreessen, J. Krieft, A. S. Shestakov, C. H. Back, J.-M. Schmalhorst, A. Hütten, G. Reiss, and T. Kuschel. Quantitative separation of the anisotropic magnetothermopower and planar nernst effect by the rotation of an in-plane thermal gradient. *Scientific Reports*, 7:40586 EP –, Jan 2017. Article.

[32] A. S. Semisalova. Magnetoresistance effects, 2017. Bad Honnef Physics School on Magnetism: From Fundamentals to Spin based Nanotechnology.

[33] J. Smit. Magnetoresistance of ferromagnetic metals and alloys at low temperatures. *Physica*, 17:612–627, June 1951.

[34] D. T. Son and B. Z. Spivak. Chiral anomaly and classical negative magnetoresistance of weyl metals. *Phys. Rev. B*, 88:104412, Sep 2013.

[35] K. Wagner, A. Kákay, K. Schultheiss, A. Henschke, T. Sebastian, and H. Schultheiss. Magnetic domain walls as reconfigurable spin-wave nanochannels. *Nature Nanotechnology*, 11:432 EP –, Feb 2016.

[36] M. Weiler, M. Althammer, F. D. Czeschka, H. Huebl, M. S. Wagner, M. Opel, I.-M. Imort, G. Reiss, A. Thomas, R. Gross, and S. T. B. Goennenwein. Local charge and spin currents in magnetothermal landscapes. *Phys. Rev. Lett.*, 108:106602, Mar 2012.

[37] Wikipedia contributors. Chirality (physics) — Wikipedia, the free encyclopedia, 2018. [Online; accessed 17-September-2018].

[38] J. Xiong, S. K. Kushwaha, T. Liang, J. W. Krizan, M. Hirschberger, W. Wang, R. J. Cava, and N. P. Ong. Evidence for the chiral anomaly in the dirac semimetal na3bi. *Science*, 350(6259):413–416, 2015.

[39] B. Yan and C. Felser. Topological Materials: Weyl Semimetals. *Annual Review of Condensed Matter Physics*, 8:337–354, Mar. 2017.

[40] J. Zak, E. R. Moog, C. Liu, and S. D. Bader. Fundamental magneto-optics. *Journal of Applied Physics*, 68:4203–4207, Oct. 1990.